Thermophysical Investigation of Asteroid Surfaces. II. Factors Influencing Grain Size

Mac Lennan, Eric Michael

2022-02

Mac Lennan , E M & Emery , J P 2022 , ' Thermophysical Investigation of Asteroid Surfaces. II. Factors Influencing Grain Size ' , The Planetary Science Journal , vol. 3 , no. 2 , 47 . https://doi.org/10.3847/PSJ/a

http://hdl.handle.net/10138/354837
https://doi.org/10.3847/PSJ/ac4967

The Planetary Science Journal, 3:47 (23pp), 2022 February https://doi.org/10.3847/PSJ/ac4967

Thermophysical Investigation of Asteroid Surfaces. II. Factors Influencing Grain Size

Eric M. MacLennan[1,2] and Joshua P. Emery[2,3]
[1] Department of Physics, P.O. Box 64, 00560FI-00560 University of Helsinki, Finland; https://www.mv.helsinki.fi/home/maceric/home.html, eric.mclenan@helsinki.fi
[2] Earth and Planetary Sciences Department, Planetary Geosciences Institute, The University of Tennessee, Knoxville, TN 37996, USA
[3] Department of Physics and Astronomy, Northern Arizona University, NAU Box 6010, Flagstaff, AZ 86011, USA
Received 2021 July 12; revised 2021 November 18; accepted 2021 December 6; published 2022 February 24

Abstract

Asteroid surfaces are subjected to mechanical weathering processes that result in the development and evolution of regolith. Two proposed mechanisms—impact bombardment and thermal fatigue—have been proposed as viable and dominant weathering processes. Previously, we compiled and estimated thermal inertias of several hundred asteroids (mostly in the main belt) for which we determined dependencies on temperature, diameter, and rotation period. In this work, we estimate grain sizes of asteroid regoliths from this large thermal inertia data set using thermal conductivity models. Following our previous work, we perform multivariate linear model fits to the grain size data set and quantify its dependency on diameter and rotation period. We find that the preferred model indicates that asteroid grain sizes are inversely dependent on object size for <10 km asteroids and exhibit no relationship above this size cutoff. Rotation period and grain size show a positive relationship when the rotation period is greater than $\sim$5 hr and an inverse relationship below this rotation period. These results indicate that both impact weathering and thermal fatigue are relevant regolith evolution mechanisms. We run post-hoc *t*-tests between spectral groups to infer the influence of composition on regolith grain sizes. We find that M-type (including suspected metal-rich objects) and E-type asteroids have larger grain sizes relative to our population sample and that P-type asteroids have distinctly smaller grains than other groups.

Unified Astronomy Thesaurus concepts: Asteroid surfaces (2209); Linear regression (1945); Asteroid belt (70); Asteroid rotation (2211); Asteroids (72); Main belt asteroids (2036); Near-Earth objects (1092)

Supporting material: machine-readable table

1. Introduction

The study and characterization of asteroid regolith—the unconsolidated, heterogeneous, rocky material covering the surface of planetary bodies (Shoemaker et al. 1969)—is an important part of understanding the processes and evolution of airless bodies of the solar system. Generally speaking, asteroid surfaces evolve from poorly sorted, blocky mixtures to well-sorted, fine-grained regolith (Hörz et al. 2020). Thermal inertia, Γ, is a thermophysical property that can be used to characterize asteroid regolith. Thermal inertias lower than that of bare rock ($\Gamma \sim 1500$–$2500\ \mathrm{J\ m^{-2}\ K^{-1}\ s^{-1/2}}$; Jakosky 1986; Bandfield et al. 2011) indicate the presence of regolith, with lower values signaling a finer-grained surface. Although some meteorites have measured thermal inertia lower than this ($\Gamma \sim 1000\ \mathrm{J\ m^{-2}\ K^{-1}\ s^{-1/2}}$; Opeil et al. 2010, 2020), the range of many asteroid thermal inertias ($<150\ \mathrm{J\ m^{-2}\ K^{-1}\ s^{-1/2}}$; MacLennan & Emery 2021, hereafter Paper I) is significantly lower. The bulk thermal inertia can be expressed as $\Gamma = \sqrt{k_{\mathrm{eff}}\,\rho_{\mathrm{grain}}\,c_s(1-\phi)}$, in which k_{eff} is the effective thermal conductivity of the regolith, ρ_{grain} is the density of a rock with no void spaces, c_s is the specific heat capacity of the material, and the regolith porosity, ϕ, is explicitly accounted for. Some mechanisms have been suggested as the primary drivers of regolith mechanical weathering on airless bodies: meteoroid impacts and thermal cycling.

Small meteoroid (<1 m) impacts can cause a breakdown of surface material over time. Some of the energy from an impact is partitioned into fragmenting near-surface material of the target body, although the exact fraction of energy that goes into this mechanical work is uncertain (Horz & Cintala 1997). Some of the energy is partitioned into launching particles off the surface on various trajectories (ejecta), which partly depend on the proximity to the impact site and on the mechanical properties of the impactor and target. Particles that do not reach escape velocity return to the surface as newly formed regolith. Other factors, such as the target porosity and strength, also play relevant roles in the production of craters and of regolith. For example, Housen & Holsapple (2003) found a clear inverse relationship between the ejecta/impactor mass ratio and porosity of the target. Impacts that excavate into fractured bedrock will generate more ejecta blocks. Thus, regolith evolution driven by impacts is dependent on the size of the body and the strength of the material, among other factors.

Internal stresses caused by differential thermal expansion, as a result of cyclic heating and cooling, lead to regolith breakdown and erosion (Eppes et al. 2015). The efficiency of this thermal cycling process has been modeled under the thermal environments of airless solar system bodies (e.g., Molaro & Byrne 2012; Molaro et al. 2017), and its feasibility has been experimentally demonstrated on meteorite samples (Delbo et al. 2014; Libourel et al. 2020). Molaro et al. (2020) demonstrated that large cracks observed on rocks seen across Bennu's surface were consistent with thermal fatigue model predictions. In general, increasing the heterogeneity of a rock (by changing the mineral grain boundaries or pores of empty space) can raise the peak stresses by up to a factor of three, compared to a homogeneous rock (Molaro et al. 2015). Thermal fracturing acts on spatial scales spanning many orders of magnitude, and modeling work has shown that the efficiency depends on heliocentric distance, rotation period, and

material thermomechanical properties (El Mir et al. 2019; Ravaji et al. 2019). The propagation of the thermal wave within a boulder initiates one or more cracks at the microscale throughout the boulder interior and throughout the diurnal cycle (Hazeli et al. 2018). These microcracks most likely originate near mineral grain boundaries, preferentially grow perpendicular to the local surface, and ultimately intersect other fractures, reaching sizes of several centimeters (Delbo et al. 2014; Molaro et al. 2015). Growth of large-scale cracks occurs in the direction of the heat flow throughout the boulder and is thus able to transverse rocks that are several times larger than the initial fracture(s). Although rapidly rotating asteroids exhibit small diurnal temperature differences, Delbo et al. (2014) showed that even a short heating cycle of 2.2 hr is sufficient to generate and grow cracks. Lastly, Molaro & Byrne (2012) claim that fast rotators ought to facilitate larger maximum thermal gradients, thus predicting a rotation period dependence of the overall efficiency.

This work (Paper II) continues our thermophysical investigation of asteroid surface properties by estimating thermally characteristic grain sizes from thermal inertias (Paper I). We use these grain sizes to study regolith evolution in the context of two proposed regolith evolution mechanisms: meteoroid impact degradation and thermal fatigue cycling. These processes have been proposed as relevant for the creation and subsequent evolution of regolith on asteroid surfaces. The relevance of each weathering mechanism can be examined by comparing the relative correlation between regolith grain size and asteroid diameter or rotation period. Specifically, we claim that if regolith development and evolution are highly dependent on meteoroid impacts, then we expect a statistically significant correlation between the grain sizes and asteroid diameters. Similarly, if thermal cycling is effective, then we should observe that grain sizes are correlated with rotation periods. These two mechanisms are not mutually exclusive; thus, we consider the possibility that both are relevant for asteroid surfaces by using a multivariate linear model in our analysis (Section 3.2). We use this multivariate model to test the following hypotheses: (1) larger asteroids exhibit evolved regoliths, quantified by smaller grain sizes, and (2) slowly rotating asteroids have a poorly developed regolith, characterized by larger grain sizes. We also investigate how the regolith properties of main belt asteroids (MBAs) are related to spectral classification using post-hoc tests of the fitted model residuals (Section 3.3) and orbital properties of near-Earth asteroids (NEAs; Section 3.4). Finally, we note that it is currently unclear in what ways these grain sizes characterize a heterogeneous mixture of, e.g., regolith grains and boulders (Figure 1). Thus, although the grain sizes estimated herein may be inaccurate in the absolute sense (Section 2.4), we utilize the modeling results to interpret the trends (Section 4) within the asteroid population in the context of regolith evolution mechanisms.

2. Methods

A handful of models have been developed for estimating grain size from thermal inertia of planetary surfaces by experimentally observing and/or theoretically modeling heat flow in granular media. For example, laboratory experiments have been able to observe empirical effects of particle size on $k_{\rm eff}$ (Watson 1964; Presley & Christansen 1997; Presley & Craddock 2006; Sakatani et al. 2018). Since, for airless planetary regoliths, Γ is primarily, but not exclusively, influenced by changes in $k_{\rm eff}$, an estimate of grain size can be made from Γ by using an appropriate thermal conductivity model for a granular medium (e.g., Gundlach & Blum 2013; Sakatani et al. 2017; Woods-Robinson et al. 2019; Wood 2020). In general, for airless bodies $k_{\rm eff}$ has a solid-state component that describes heat conduction through grains and across grain contacts and a radiative component that describes heat radiated across pore spaces (e.g., Watson 1964):

$$k_{\rm eff} = k_{\rm solid} + k_{\rm rad} = k_1(T) + k_2 T^3. \quad (1)$$

The k_1 and k_2 coefficients in Equation (1) are dependent on the material properties of the regolith, such as grain size, packing fraction, and amount of contact between the grains (Watson 1964). Note that the solid component of thermal conductivity is temperature dependent and varies with composition (Wood 2020, and references therein). These coefficients are approximated in the works of Gundlach & Blum (2013) and Sakatani et al. (2017), from which measurements of Γ (combined with the compositional information about the asteroid) can be used to estimate a characteristic grain size for an asteroid. We thus employ both these models, with an anisothermality correction from Ryan et al. (2020) applied to the radiative conductivity term, to estimate characteristic regolith grain sizes for each asteroid.

The Gundlach & Blum (2013) formulations of k_1 and k_2 are calibrated using laboratory heat-flow measurements of lunar regolith (Chan & Tien 1973; Gundlach & Blum 2012). On the other hand, Sakatani et al. (2017) used mixtures of powdered glass beads of varying sizes and porosities. The surface temperature is required input for these models, from which we use the color temperature reported in Paper I. These models also need compositional information about the material, which we infer from the asteroid's spectral taxonomic type when available. For objects for which there is no spectral information available, we infer the spectral type from the geometric albedo. Many asteroids belong to a dynamical family (Table 1), in which case we can infer the spectral type and perform a cross-check with the geometric albedo or reflectance spectrum, if available. We assign a meteorite analog to each spectral type as outlined in Section 2.2 and account for uncertainties in the thermal inertia and various material properties by using a Monte Carlo method (Section 2.3) when implementing the model.

2.1. Thermal Conductivity Modeling

The solid thermal conductivity component, k_1, is modeled by Gundlach & Blum (2013) via computing the efficiency of heat transfer through the surface contacts within a network of grains:

$$k_1^{\rm G\&B} = k_{\rm grain}\frac{r_c}{r_g}(f_1\ \exp([f_2\psi])\ \Xi. \quad (2)$$

Here $k_{\rm grain}$ is the thermal conductivity of a grain with zero porosity and $\psi = 1-\phi$ is the volume filling factor (packing fraction). The empirically derived constants $f_1 = (5.18 \pm 3.45) \times 10^2$ and $f_2 = 5.26 \pm 0.94$ encapsulate information about the path of contact chains in the direction of heat flow (Gundlach & Blum 2012). Thermal conductivity measurements of Apollo 11 and 12 samples are used to estimate $\Xi = 0.41 \pm 0.02$, which incorporates and accounts for the irregular shapes of the particles and heterogeneity of regolith on the whole. The

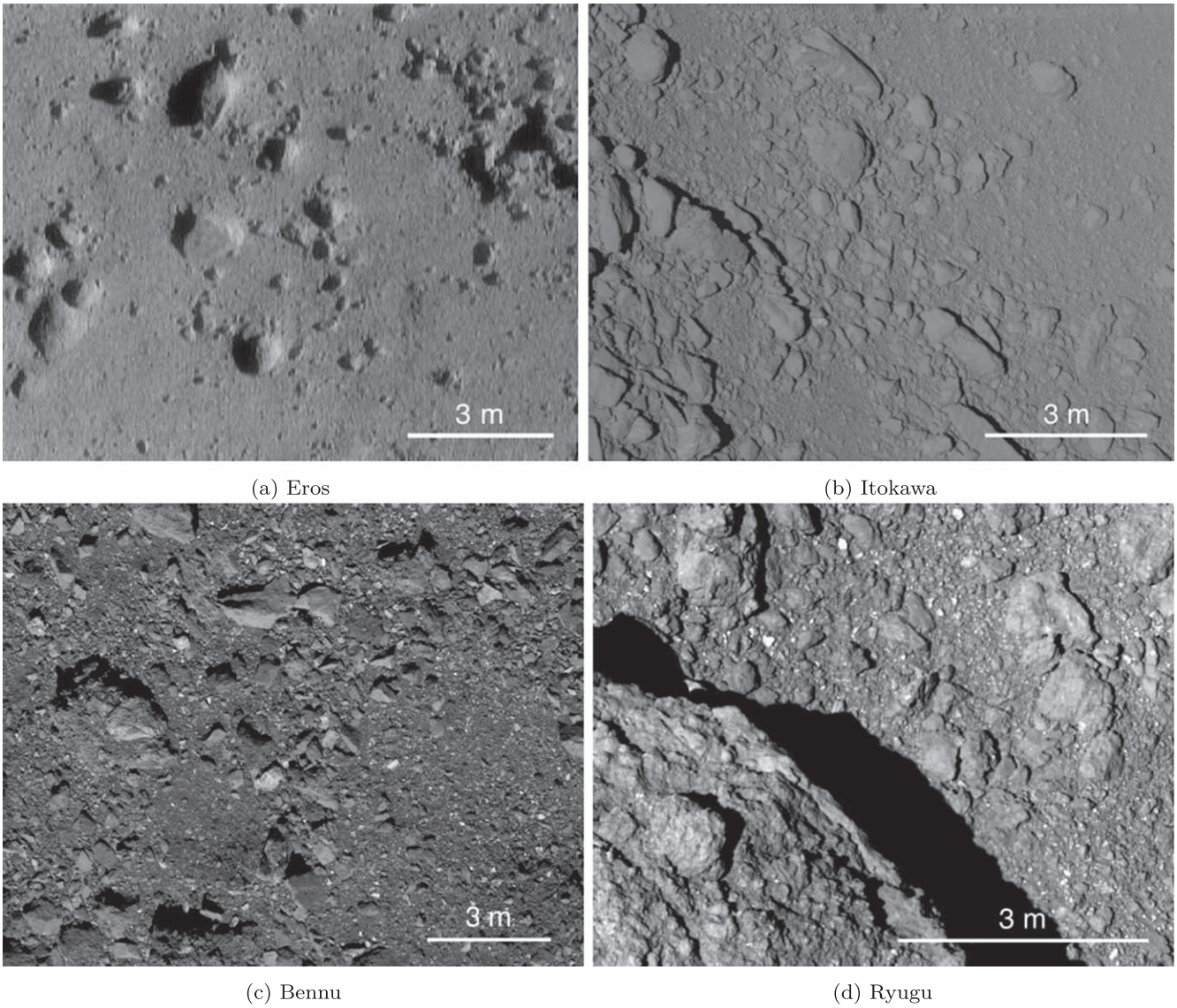

(a) Eros (b) Itokawa

(c) Bennu (d) Ryugu

Figure 1. Spacecraft images of the regolith on Eros, Itokawa, Bennu, and Ryugu acquired by the NEAR, Hayabusa, OSIRIS-REx, and Hayabusa 2 missions, respectively.

factors contained within brackets in Equation (2) approximate the adhesive forces between regolith grains, which dominate over gravity on small bodies, to estimate the contact area between them. The contact radius between grains, r_c, is calculated by Johnson–Kendall–Roberts theory (Johnson et al. 1971), assuming that adhesive forces are dominant:

$$r_c = \left[\frac{9\pi}{4}\frac{(1-\nu^2)}{E}\gamma(T)r_g^2\right]^{-1/3}, \quad (3)$$

where ν is Poisson's ratio, E is Young's modulus, and $\gamma(T) = T \cdot 6.67 \times 10^{-5}\,\mathrm{J\,m^{-2}}$ is the specific surface energy of each grain—a measure for the adhesive bonding strength between grains.

In Sakatani et al. (2017), the solid conductivity component is modeled in a similar way to the formula above:

$$k_1^{\mathrm{Sak}} = k_{\mathrm{grain}}\frac{r_c}{r_g}\frac{4\psi C\xi}{\pi^2}, \quad (4)$$

where r_c is the contact radius, also represented by Equation (3). The coordination number,

$$C = \frac{2.8112(1-\phi)^{-1/3}}{f^2(1+f^2)}, \quad (5)$$

is the average number of particles that are in contact with each other and is a function of the regolith porosity. Here $f = 0.07318 + 2.193\phi - 3.357\phi^2 + 3.914\phi^3$. The factor ξ is dependent on the shape and smoothness of the particles and is equal to unity for perfectly smooth spheres. We use $\xi = 0.4$, which approximates rough, nonspherical particles and is well within the range of experimentally derived values from Sakatani et al. (2017).

The radiative thermal conductivity (k_{rad}) coefficient is calculated by Gundlach & Blum (2013) to be

$$k_2^{\mathrm{G\&B}} = 8\epsilon\sigma_0 e_1\frac{1-\psi}{\psi}r_g, \quad (6)$$

with the bolometric emissivity, ϵ, Stefan–Boltzmann constant, $\sigma_0 \approx 5.6710^{-8}$ W m^{-2} K^{-4}, and the empirically derived coefficient $e_1 = 1.34 \pm 0.01$ (Dullien 1979; Gundlach & Blum 2012). The mean free path of a photon between regolith grains is directly proportional to their size, hence the r_g factor in Equation (6). In Sakatani et al. (2017) the radiative heat transfer coefficient is calculated via

$$k_2^{\mathrm{Sak}} = 8\sigma_0\zeta\frac{\epsilon}{2-\epsilon}\left[\frac{1-\psi}{\psi}\right]^{1/3} r_g, \quad (7)$$

where ζ is an enhancement factor for which we use $\zeta = 1.7$—an average of the experimentally derived values in Sakatani et al. (2017). However, we note that k_{rad} values presented in Sakatani et al. (2017) show a clear inverse dependency on r_g, which may be related to the effect of short-range (immediately adjacent) versus long-range (nonadjacent) radiation exchange that is dependent on the particle size (van Antwerpen et al. 2012).

Thermal gradients that exist within individual regolith particles cause a nonlinear relationship between r_g and k_{rad} (Ryan et al. 2020). Such thermal gradients will arise in large particles, when the solid component of thermal conductivity is low, or for particles that have significant intragranular porosity. In these cases, the radiative component of thermal conductivity will be less than the T^3 theoretical relationship. Building off the work of van Antwerpen et al. (2012), Ryan et al. (2020) use the dimensionless parameter Λ_s in an updated version of the nonisothermal correction factor, f_k:

$$\Lambda_s = \frac{k_{\mathrm{grain}}}{8 r_g \sigma_0 T^3} \quad (8)$$

and

$$f_k = a_1 \tan^{-1}(a_2 \Lambda_s^{-a_3}) + a_4. \quad (9)$$

When $\Lambda_s > 25$, f_k is set to unity; otherwise, f_k can be calculated via Equation (9), where $a_1 = -0.568$, $a_2 = 0.912$, $a_3 = 0.765$, and $a_4 = 1.035$. To account for this nonisothermality, we multiply the coefficients calculated in Equations (6) and (7) by f_k.

2.2. Input Parameters

Some of the required input parameters to the equations listed above are dependent on the composition of the material. Since meteorites are samples of asteroids, we attempt to establish a meteorite analog that is most appropriate for each asteroid in this study. The most direct approach can be made when high-quality spectra have been acquired for an object. Various taxonomic systems have been defined based on photometric colors and albedos (Tholen 1984), or absorption features with spectral slopes of reflectance spectra (Bus & Binzel 2002; DeMeo et al. 2009). The taxa defined in these works relate to different compositions, although connections can be ambiguous in many cases, particularly for featureless spectra. Visible spectra and color information can be used to broadly distinguish between the S-complex (any spectral taxon beginning with an "S" and Q-types that are the unweathered endmember), K-type, V-type, B-type, C-complex (any taxon beginning with a "C"), and Bus-DeMeo X-complex. For the X-complex we adopt the Tholen (1984) E-, M-, and P-type system, whose components are distinguished by their geometric albedos. We use *V*-band geometric albedo cutoff of $p_V \gtrsim 0.42$ for E-type objects, $0.12 < p_V < 0.42$ for M-type objects, and $p_V \lesssim 0.12$ for P-type objects.

Many asteroids in our sample have no color or spectral information available; thus, we are left to infer their compositional information by other means. For this exercise we use the geometric albedo reported and compiled in Paper I and *V*-band slope parameters (G_V) from Oszkiewicz et al. (2011), which have both been shown to correlate with spectral class (e.g., Oszkiewicz et al. 2012; Vereš et al. 2015). We found that using cutoff criteria only for p_V was sufficient, but we still utilize G_V values as a consistency check that each object is within the range of expected values for its spectral class. All objects' p_V and G_V values are included in Figure 2. It is interesting to note the positive correlation between p_V and G_V for the entire data set (across taxonomic groups), yet within each taxonomic group this correlation is absent or exhibits an inverse relationship. Such a scenario is an example of Simpson's statistical paradox[4] (Yule 1903; Simpson 1951). We briefly note this paradox for possible future investigations of p_V, G_V, and regolith grain-scale size across different spectral/compositional groups.

To distinguish between high-albedo S-complex and low-albedo C-complex, we use $p_V = 0.12$, whereas objects with $p_V > 0.45$ are assumed to be E-types. The $p_V = 0.12$ cutoff value is consistent with DeMeo & Carry (2013), who present average albedos for different asteroid taxa using a larger sample size than ours. This cutoff criterion is also consistent with laboratory-derived geometric albedos of ordinary chondrites and CO, CM, and CI carbonaceous chondrites (Figure 7 of Beck et al. 2021). However, the laboratory-derived values for CK and CV chondrites have significant overlap with unequilibrated (type 3) ordinary chondrites for $0.12 < p_V < 0.17$. Thus, with this criterion, meteorite analog associations for eight objects in our sample with albedos in this range are considered to be ambiguous.

We assign ordinary chondrite and carbonaceous chondrite material properties to S-complex (including one O-type) and C-complex (excluding Ch-type) asteroids, respectively. We associate the low-density CM chondrites with Ch- and B-type asteroids and CI chondrites with P-type asteroids. Our object set contains a few D-types (color or spectral classification) for which we assume a P-type composition that most likely reflects the primitive compositions of these asteroids. Asteroids classified as K-type (and Xk-type) have been shown to be related to CO, CV, and CK carbonaceous chondrite meteorite groups (Burbine et al. 2001; Clark et al. 2009) and can mostly be found among the Eos family (Mothé-Diniz 2008) in our sample (Table 1). The V-type association to the howardites, eucrites, and diogenites (HEDs), a basaltic achondrite meteorite class, has been well established. Finally, the E-type (Tholen) and Xe-type (Bus-DeMeo) asteroids have a well-established connection to aubrites (enstatite achondrites) because of their high albedos (Clark et al. 2004).

Enstatite chondrites, which have a distinct thermal conductivity compared to other meteorite groups (Figure 3), have been suggested as an analog to the M-types (Clark et al. 2004). On the other hand, M-types that have a high radar albedo and thermal inertia are suggestive of a relatively high FeNi metal content (e.g., Magri et al. 1999). Spectroscopic modeling of the largest M-type, (16) Psyche, indicates a regolith composed of a

[4] Simpson's paradox describes a situation in which a data set exhibits correlations across the entire sample that are statistically distinguishable from sample correlations within groups.

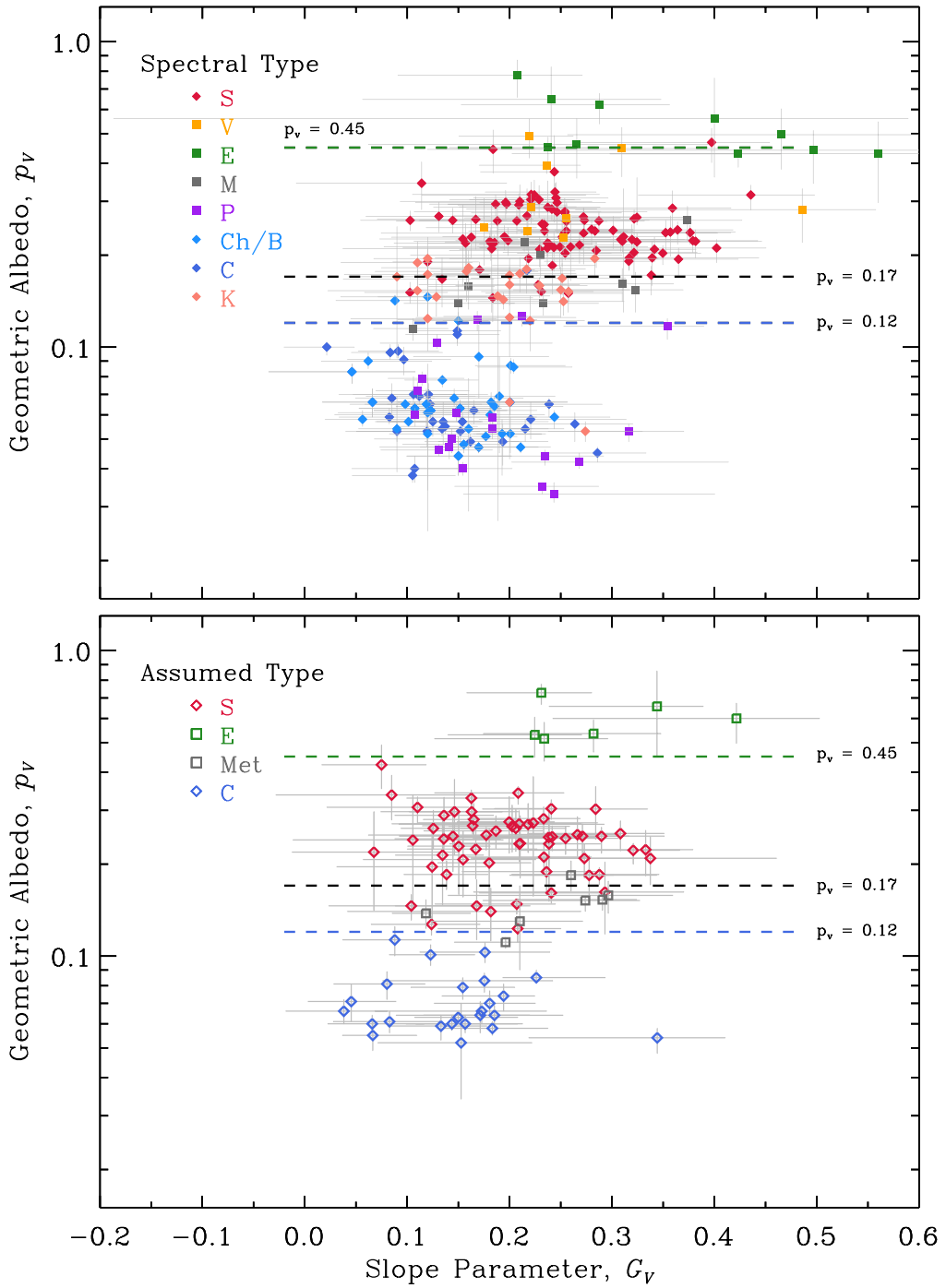

Figure 2. Geometric albedo (p_V) vs. slope parameter (G_V) grouped by spectral type for all asteroids in this study. The top panel (filled symbols) shows the objects classified on the basis of spectral or color data and family membership, when applicable. The bottom panel (open symbols) shows the objects classified only on the basis of albedo.

silicate-metal mixture with exogenous carbonaceous material (Landsman et al. 2018; Cantillo et al. 2021)—the former being consistent with results for smaller M-types (Sanchez et al. 2021). The Psyche mission (Elkins-Tanton et al. 2016) should reconcile the various thermal inertia estimates[5] that range from <100 J m^{-2} K^{-1} s$^{-1/2}$ (Landsman et al. 2018) up to 210 ± 60 J m^{-2} K^{-1} s$^{-1/2}$ (de Kleer et al. 2021) with the spectroscopic evidence and provide crucial information (i.e., porosity, emissivity, and metal content) that can be used to model the surfaces of other suspected metal-rich M-types. Although we assume a purely metal surface for all suspected metal-rich asteroids, which is most likely an inaccurate assumption, we show in Section 2.4 that this assumption does not drastically affect the grain size estimate.

The thermal conductivity ($k_{\rm grain}$), grain density ($\rho_{\rm grain}$), heat capacity (c_s), Young's modulus (E), and Poisson's ratio (μ) for all aforementioned groups are shown in Table 4. In the

[5] We clarify that we have chosen to use Psyche's thermal inertia that was obtained by Matter et al. (2013), which is based on disk-resolved, mid-infrared observations—a wavelength range that is comparable to most other thermal inertias used for this work.

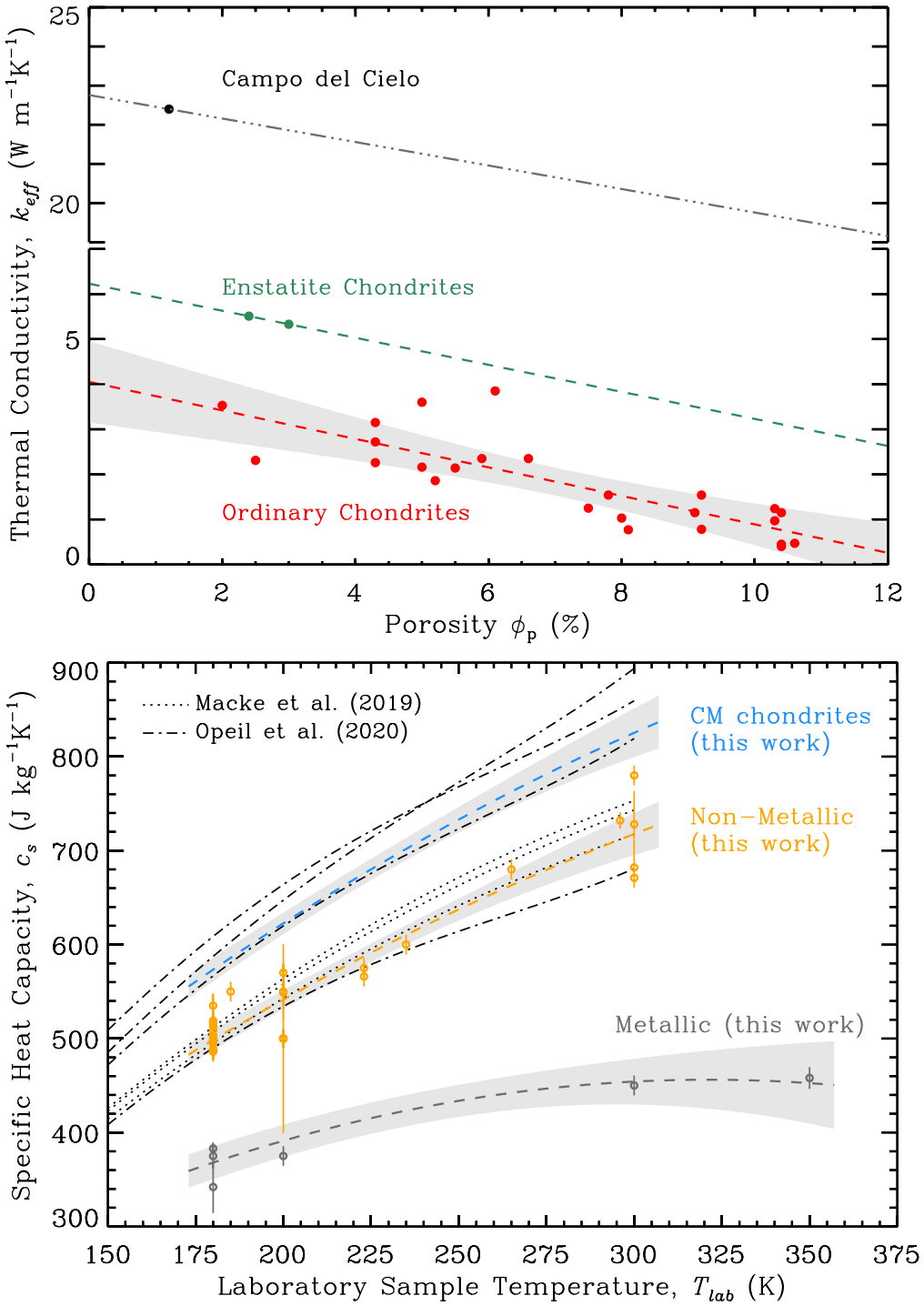

Figure 3. Meteorite thermal conductivity as a function of porosity (top; Table 2) and specific heat capacity as a function of temperature (bottom; Table 3). Dashed lines from this work show linear fits in the top panel and parabola fits through the origin in the bottom panel, with gray regions representing 95% confidence to the fits. The dashed–dotted line through the Campo del Cielo datum in the top panel assumes a slope of 0.3. Note the break in the *y*-axis in the top panel.

following subsections, we describe how these properties were chosen for each spectral group and analyze data from many sources, when appropriate, to account for temperature and porosity effects. We note that, in our albedo-based classification, M-types and low-albedo V-types could potentially be misclassified as S-types, and, similarly, some P-types may be misclassified as C-types. However, we see no obvious reason to reassign any of these S-types to the M-type group, as their thermal inertias are inconsistent with a high thermal conductivity, which would otherwise suggest a metal-rich surface. On the other hand, some P-types might be misclassified as C-types. We change the classification of (4003) Schumann from C-type to P-type, based on its location in the outer part of the main belt (≈3.4 au), where P-types are more abundant than C-types (DeMeo & Carry 2013, 2014). The difference in assumed material properties between C- and P-types that we use is not large and would not alter the reported grain size by more than a few percent.

Table 1
Asteroid Family Properties

PDS Family ID	AstDyS Family ID	Num	Spec.	Collision Type[a]/Note	Count[b]
003 Hungaria	(434) Hungaria	2965	Xe/E	Fragmentation	6
		Inner Main Belt			
401 Vesta	(4) Vesta	15252	V	Cratering	14[c]
402 Flora		13786	S		25[c]
403 Baptistina	(883) Matterania	2500	S	cluster within Flora	3[c]
404 Massalia	(20) Massalia	6424	S	Cratering	1[c]
405 Nysa-Polana high-pV)			S		8
405 Nysa-Polana (low-pV)			C		3
415 Chaldaea		1776	Ch		2
416 Svea		48	C/B		1[c]
701 Phocaea	(25) Phocaea	1989	S		10
		Middle Main Belt			
502 Eunomia	(15) Eunomia	5670	S	Cratering	14
505 Adeona	(145) Adeona	2236	C		3
506 Maria	(170) Maria	2940	S		4
507 Padua	(363) Padua/(110) Lydia	1087	X/P	Fragmentation	1
509 Chloris	(410) Chloris	424	C		2
512 Dora	(668) Dora	1259	C	Fragmentation	2[c]
513 Merxia	(808) Merxia	1215	S	Fragmentation	2[c]
516 Gefion	(93) Minerva	2547	S		2[c]
519 Hoffmeister	(1726) Hoffmeister	1819	C	Fragmentation	1
531 Mitidika		653			2
	(5) Astraea	6169	S?	Cratering	3
		Outer Main Belt			
601 Hygiea	(10) Hygeia	4854	C	Cratering	7[c]
602 Themis	(24) Themis	4782	C	Fragmentation	9[c]
603 Sylvia	(87) Sylvia	255	X/P		1[c]
604 Meliboea		444	C		2
605 Koronis	(158) Koronis	5949	S	Fragmentation	16
606 Eos	(221) Eos	9789	K	Fragmentation	23
607 Emma	(283) Emma	76	C	Cratering	1[c]
609 Veritas	(490) Veritas	1294	C		1
610 Karin		541	S	cluster within Koronis	2
620 Beagle	(656) Beagle	148	C	cluster within Themis	1[c]
631 Ursula	(375) Ursula	1466	C/X?		1
633 Itha		54	S		1[c]
634 Inarradas		38			1[c]
902 Alauda		1294	B?		3
		Hilda Group			
002 Schubart	(1911) Schubart	352	P	Fragmentation	1

Notes.
[a] Collisional type definitions from Milani et al. (2015).
[b] Number of asteroid family members present in this study.
[c] Largest family member appears in this study.

2.2.1. Thermal Conductivity

Laboratory measurements of meteorite thermal conductivities reveal dependence on the material porosity and temperature. In their review paper of thermal conductivites, Flynn et al. (2018) show that laboratory measurements of thermal conductivity do not change significantly in the temperature range from 100 to 300 K but approach zero at 0 K. Additionally, void spaces can significantly impede the net solid-state heat flow within a meteorite sample (Soini et al. 2020). To account for porosity effects, we estimate the thermal conductivity at zero porosity using data collected at the same temperature.

In order to estimate thermal conductivity at $\phi = 0$, lines are fit to meteorite samples with porosities less than 12% from the literature (Table 2), as shown in Figure 3. Since the carbonaceous chondrites with measured $k_{\rm eff}$ had porosities exceeding this cutoff, we did not use any for our analysis. We found that enstatite chondrites have a larger thermal conductivity than the ordinary chondrite samples (and one Shergottite), likely due to mineralogical differences. The y-intercept of the best-fit lines gives the thermal conductivity at zero porosity of 4.05 and 6.23 W $m^{-1} K^{-1}$ for ordinary chondrites and enstatite chondrites, respectively. Because the thermal conductivity for terrestrial enstatite is 90% that of enstatite chondrites at 275 K, we scale the function downward by 10% to approximate the aubrite thermal conductivity, which is mostly composed of enstatite. We used the same linear slope to extrapolate a single measurement of thermal conductivity

Table 2
Meteorite Thermal Conductivity Measurements at 200 K

Sample	Group	ϕ[a]	k_{eff}[b]	Source
ALH 77288	H6	2.0	3.53	Yomogida & Matsui (1983)
Arapahoe	L5	2.5	2.31	Yomogida & Matsui (1983)
Bath Furnace 1	L6	4.3	2.26	Opeil et al. (2012)
Bath Furnace 2	L6	4.3	2.72	Opeil et al. (2012)
Bath Furnace 3	L6	4.3	3.15	Opeil et al. (2012)
Bruderheim	L6	8.0	1.03	Yomogida & Matsui (1983)
Farmington	L5	5.5	2.14	Yomogida & Matsui (1983)
Gilgoin Station	H5	5.0	3.60	Yomogida & Matsui (1983)
Gladstone	H5	5.0	2.16	Yomogida & Matsui (1983)
Holbrook 1	L6	10.4	0.45	Opeil et al. (2012)
Holbrook 2	L6	10.4	1.15	Opeil et al. (2012)
Kunashak	L6	5.2	1.86	Yomogida & Matsui (1983)
Leedey,A	L6	10.4	0.40	Yomogida & Matsui (1983)
Leedey,B	L6	10.6	0.47	Yomogida & Matsui (1983)
Los Angeles	Sher[c]	8.1	0.77	Opeil et al. (2012)
MET 78003	L6	7.8	1.54	Yomogida & Matsui (1983)
Monroe	H4	5.9	2.35	Yomogida & Matsui (1983)
New Concord	L6	9.2	0.78	Yomogida & Matsui (1983)
Pultusk	H5	7.5	1.25	Opeil et al. (2012)
Wellman	H5	6.1	3.85	Yomogida & Matsui 1983
Y-74156	H4	9.2	1.54	Yomogida & Matsui (1983)
Y-74191	L3	10.3	1.24	Yomogida & Matsui (1983)
Y-74647	H4.5	9.1	1.15	Yomogida & Matsui (1983)
Y-75097	L4	10.3	0.97	Yomogida & Matsui (1983)
Abee	EH4	3.0	5.33	Opeil et al. (2010)
Pillistfer	EL6	2.4	5.51	Opeil et al. (2012)
Campo del Cielo	IAB	1.2	22.4	Opeil et al. (2010)

Notes.
[a] Sample porosity (%).
[b] Effective thermal conductivity (W m^{-1} K^{-1}).
[c] Shergottite meteorite group (Martian origin).

(Opeil et al. 2010) of the FeNi meteorite Campo del Cielo to estimate the thermal conductivity at $\phi = 0$ that is used in the thermal conductivity model to compute grain size.

Data presented by Soini et al. (2020) show that the thermal conductivities of ordinary and carbonaceous chondrites are in agreement when the sample porosities are taken into account. Because we account for sample porosities and are using grain densities, we use the same zero-porosity thermal conductivity value for carbonaceous chondrites and ordinary chondrites, with the exception of CM chondrites. Newer thermal conductivity measurements of CM chondrites from Opeil et al. (2020) are also consistent with other carbonaceous chondrites. However, the spacecraft observations of B-type Bennu and Cg-type Ryugu revealed surfaces with weak, low-conductivity boulders that have thermal inertias that are ~2–3 times smaller than stronger, high-conductivity boulders (Grott et al. 2019; Rozitis et al. 2020). This stronger material may be identical to CM chondrites found on Earth, yet the weak material is likely less abundant among meteorite collections (Popova et al. 2011). In order to account for the presence of this weak material that is likely present on Ch- and B-type asteroids, we adopt a lower thermal conductivity for both. Because this weaker material is most likely primitive in origin, we assign the low thermal conductivity to CI chondrites as well.

Our computed thermal conductivity values agree with the Soini et al. (2020) model fits to essentially the same data set as ours. We accounted for temperature-dependent thermal conductivity among these samples by bootstrapping our k_{grain} calculations with the data compiled in Flynn et al. (2018). Ordinary chondrites, HEDs, and carbonaceous chondrites do not demonstrate a significant dependence on temperature (Opeil et al. 2012; Flynn et al. 2018) in the range relevant to this study, so we use constant values. For FeNi and enstatite chondrite curves, we scale the curves presented in Figure 15 of Flynn et al. (2018) to our values of k_{grain} at 200 K. FeNi meteorites show a roughly linear dependence, and enstatite chondrites (and by deduction, the enstatite-dominated aubrites) show an inverse dependence on temperature. These temperature-dependent k_{grain} functions, which are valid for 200–350 K, are listed in Table 4 and are assigned a 10% uncertainty in the thermal conductivity model.

2.2.2. Grain Density and Heat Capacity

Meteorite specimens, while not regolith, still contain small pores and cracks that lower the bulk density of the sample (e.g., Cadenhead & Stetter 1975). These microporosities, ϕ, range from 4% to 10% but can be as high as 20% for weathered fines and as low as 2% for iron meteorites. We wish to use the grain density (ρ_{grain}), the density of a material with zero porosity, as input to the thermal conductivity models. We primarily use the findings of Macke (2010), who measured the porosities of individual meteorites with various compositions and computed ρ_{grain}. Table 4 lists grain densities for many meteorite analogs related to their respective spectral types. For the S-complex and V-types we use a uniform distribution for ρ_{grain} that spans the values reported in Macke (2010), instead of a normal distribution.

The ability of material to store thermal energy per unit mass is quantified by its specific heat capacity, c_s. Laboratory heat capacity measurements of several meteorites reveal a clear temperature dependence (Beech et al. 2009; Opeil et al. 2012, 2020; Szurgot et al. 2012; Consolmagno et al. 2013; Wach et al. 2013; Macke et al. 2019). We account for this dependence by performing an independent meta-analysis—similar to that on the thermal conductivity data set above—in which we use literature data on meteorite heat capacities measured at various ambient temperatures. While Flynn et al. (2018) perform a similar analysis, they present fits for a temperature range of 75–200 K, which does not cover the full range of asteroid surface temperatures found in this work. Our empirical fits to the data are in agreement with the semiempirical functions of Macke et al. (2019), who used a larger data set. Our results are very similar to theirs over the same temperature range.

Opeil et al. (2020) present temperature-dependent heat capacities for five CM chondrites, which we compare our results to below. We compute second-order polynomial fits to the data shown in Table 3 over a temperature range of 175–300 K and with a y-intercept fixed at zero (because at low temperatures the heat capacity approaches zero). Among our data set, we find that two distinct trends emerge, forming two groupings: one with all the iron-nickel meteorites (metallic) and one composed of all chondritic and achondritic meteorites (nonmetallic). The best-fit heat capacity equations (and coefficient uncertainties) for nonmetallic and metallic meteorites at different temperatures are given by $c_s = -0.0033$

Table 3
Meteorite Heat Capacity Measurements at Different Ambient Temperatures

Sample	Type	T_{lab} (K)	c_s (J kg^{-1} K^{-1})	Source
Abee	EH4	200	500 ± 10	Yomogida & Matsui (1983)
Allende	CV	180	501 ± 21	Consolmagno et al. (2013)
Bilanga	Di.	180	509 ± 26	Consolmagno et al. (2013)
Bori	L6	180	495 ± 8	Consolmagno et al. (2013)
Cronstad	H5	200	550 ± 10	Yomogida & Matsui (1983)
Cold Bokkeveld	CM2	200	500 ± 100	Yomogida & Matsui (1983)
Cumberland	Aub.[a]	180	513 ± 14	Consolmagno et al. (2013)
Gao-Guenie	H5	296	732 ± 8	Beech et al. (2009)
Hedjaz	L3.7-6	180	488 ± 12	Consolmagno et al. (2013)
Holbrook	L6	180	486 ± 9	Consolmagno et al. (2013)
Los Angeles	Sher.[b]	185	550 ± 10	Opeil et al. (2012)
Los Angeles	Sher.[b]	300	780 ± 10	Opeil et al. (2012)
Los Angeles	Sher.[b]	235	600 ± 10	Opeil et al. (2012)
Los Angeles	Sher.[b]	265	680 ± 10	Opeil et al. (2012)
Lumpkin	L6	200	570 ± 10	Yomogida & Matsui (1983)
Ness Country	L6	180	517 ± 6	Consolmagno et al. (2013)
NWA 2086	CV	180	519 ± 28	Consolmagno et al. (2013)
NWA 4293	H6	180	498 ± 7	Consolmagno et al. (2013)
NWA 4560	LL3.2	223	566 ± 10	Wach et al. (2013)
NWA 4560	LL3.2	300	682 ± 10	Wach et al. (2013)
NWA 5515	CK4	200	500 ± 10	Yomogida & Matsui (1983)
Ornans	CO	180	497 ± 7	Consolmagno et al. (2013)
Pipe Creek	H6	180	489 ± 10	Consolmagno et al. (2013)
Pultusk	H5	180	496 ± 8	Consolmagno et al. (2013)
Renazzo	CR	180	535 ± 12	Consolmagno et al. (2013)
Soltmany	L6	200	549 ± 30	Szurgot et al. (2012)
Soltmany	L6	300	728 ± 35	Szurgot et al. (2012)
Soltmany	L6	223	575 ± 10	Wach et al. (2013)
Soltmany	L6	300	671 ± 10	Wach et al. (2013)
Thuathe	H4-5	180	487 ± 9	Consolmagno et al. (2013)
Warrenton	CO	180	503 ± 16	Consolmagno et al. (2013)
Auggustinovka	IIIAB	180	375 ± 13	Consolmagno et al. (2013)
Campo del Cielo	IAB	200	375 ± 10	Opeil et al. (2010)
Campo del Cielo	IAB	300	450 ± 10	Opeil et al. (2010)
Estherville	Meso[c]	180	383 ± 6	Consolmagno et al. (2013)
Pirapora	IIIAB	180	342 ± 27	Consolmagno et al. (2013)
Sikhote-Alin	Fe IIAB	350	458 ± 11	Beech et al. (2009)

Notes.
[a] Aubrite.
[b] Shergottite meteorite (Martian origin).
[c] Mesosiderite.

$(\pm 0.0004) \times T^2 + 3.39\ (\pm 0.10) \times T$ and $c_s = -0.0044\ (\pm 0.0004) \times T^2 + 2.84\ (\pm 0.11) \times T$, respectively. Results are shown in Figure 3, and the fits from Macke et al. (2019) and Opeil et al. (2020) are included for comparison. Because the Opeil et al. (2020) CM chondrite data set clearly exhibits higher heat capacities than our fits to other nonmetallic meteorites, we use the function $c_s = -0.0036 \times T^2 + 3.84 \times T$ for Ch- and B-type asteroids, which is calculated as 115% of the fit to the nonmetallic meteorites. As shown in Figure 3, this scaled function falls in the range of formulae presented by Opeil et al. (2020).

2.2.3. Mechanical Properties and Emissivity

Young's modulus (E) and Poisson's ratio (ν) are used in the thermal conductivity model to calculate the contact area between grains within a regolith. In particular, these two quantities are used to approximate the deformation both along the axis of an applied force and in the orthogonal dimensions. For M-type asteroids, we use the values of these properties measured for Fe–Ni alloys, which are similar to iron meteorites, by Ledbetter & Reed (1973). Ibrahim (2012) reports Young's modulus and bulk modulus (G) for many ordinary and carbonaceous chondrite meteorites. We calculate Poisson's ratio using the relationship between the three variables: $\nu = \frac{E}{2G} - 1$. This equation assumes isotropic material properties and is also used to propagate the reported E and G uncertainties presented in Ibrahim (2012). The values for E-type asteroids are assumed to be the same as used for S-types, as indicated by italics in Table 4.

Emissivity values of meteorites and terrestrial rocks cluster around 0.9—the value that we adopt in this work for all spectral groups with the exception of suspected metal-rich asteroids. Laboratory and modeling efforts by Sih & Barlow (2004) place the emissivity of powdered and solid iron roughly in the range of 0.5–0.8 for temperatures of 200–300 K. Gundlach & Blum (2013) assume an emissivity for metal-rich asteroids of 0.66, which we adopt here.

Table 4
Material Properties of Meteorite Groups

Spectral Group	Material Analog	$k_{\rm grain}$ (W m^{-1} K^{-1})	$\rho_{\rm grain}$ (kg m^{-3})	c_s[a] (J kg^{-1} K^{-1})	ϵ_g	E (GPa)	ν[b]
S-complex	Ordinary chondrites	4.05 ± 0.35	3180–3710[c]	$-0.0033 \times T^2 + 3.39 \times T$	0.9	28.8 ± 2.4[d]	0.23 ± 0.04[e]
V-type	HEDs	4.05 ± 0.35	3180–3440[f]	$-0.0033 \times T^2 + 3.39 \times T$	0.9	28.8 ± 2.4[d]	0.23 ± 0.04[e]
E-type	Aubrites	$4.28 + 258/T$ ($\pm$10%)	3150 ± 20[f]	$-0.0033 \times T^2 + 3.39 \times T$	0.9	*28.8 ± 2.4*	*0.23 ± 0.04*
M-type	E chondrites	$4.76 + 287/T$ ($\pm$10%)	3635 ± 35[g]	$-0.0033 \times T^2 + 3.39 \times T$	0.9	*28.8 ± 2.4*	*0.23 ± 0.04*
Met (high-Γ M-type)	FeNi metal	$12.4 + 0.05 \times T$ ($\pm$10%)	7500 ± 200[h]	$-0.0042 \times T^2 + 2.77 \times T$	0.66	169–209[i]	0.27–0.37[i]
P-type	CI chondrites/low k	1.5 ± 0.5	2420 ± 40[j]	$-0.0033 \times T^2 + 3.39 \times T$	0.9	18.9 ± 3.7[d]	0.14 ± 0.06[e]
C-complex	Carb. chondrites	4.05 ± 0.35	3520 ± 130[j]	$-0.0033 \times T^2 + 3.39 \times T$	0.9	18.9 ± 3.7[d]	0.14 ± 0.06[e]
Ch/B-type	CM chondrites/low k	1.5 ± 0.5	2940 ± 40[j]	$-0.0036 \times T^2 + 3.84 \times T$	0.9	18.9 ± 3.7[d]	0.14 ± 0.06[e]
K-type	CK/CO/CV chondrites	4.05 ± 0.35	3520 ± 60[j]	$-0.0033 \times T^2 + 3.39 \times T$	0.9	18.9 ± 3.7[d]	0.14 ± 0.06[e]

Notes. Choices for the thermal conductivity, heat capacity, and emissivity values are explained in Section 2.2. Italicized values are taken from S-complex values. Low k refers to weak, low-conductivity material that is not represented in meteorite collections.
[a] All calculated specific heat capacities are assigned a 10% uncertainty.
[b] Poisson's ratio.
[c] Macke (2010).
[d] Ibrahim (2012).
[e] Calculated from E and G values presented in Ibrahim (2012).
[f] Macke et al. (2011a).
[g] Macke et al. (2010).
[h] Average using data from Consolmagno et al. (2008), Opeil et al. (2010), and Szurgot et al. (2012).
[i] Ledbetter & Reed (1973).
[j] Macke et al. (2011b).

2.3. Monte Carlo Implementation

We compute a thermal conductivity, $k_{\rm eff}^{\rm obs}$, that is empirically derived from Γ and assumed values of c_s, $\rho_{\rm grain}$, and a range of porosities. This value is equated to the theoretically modeled thermal conductivity calculated using the above procedure, in order to obtain an estimated regolith grain size. Most input variables are taken from a distribution that is generated based on the uncertainty of that parameter given in Table 4 and mentioned above. Most parameters have associated 1σ uncertainties from which we generate Gaussian probability distributions. The porosity is one exception, for which we use a uniform random distribution from 0.276 to 0.876; the lower value is the porosity of the close-hexagonal packing scheme for identical spheres, and the upper value represents the hypothesized porosity of cometary regolith (i.e., Sunshine et al. 2016, and references therein). For each iteration, a single grain size is produced, ultimately constructing a distributed set of 10,000 grain sizes. For some trials, the combination of input parameters produced model thermal conductivity values that are incompatible with the observed value. These cases are therefore not included in the final distribution and are instead replaced by additional, successful trials. We note that failed trails are indicative of input parameters that fall at the tail ends of the adopted distributions and do not necessarily imply incorrect assumptions with the models.

Output grain sizes are transformed into the logarithmic scale developed by Krumbein & Aberdeen (1937), which allows for the comparison of sediment sizes across many orders of magnitude. These Krumbien *phi-scale* grain sizes, $d_{g\phi}$, are referenced from 1 mm. The output grain diameters, $d_g = 2r_g$, are transformed into this scale with

$$d_{g\phi} = -2 \log_2(d_g/1\ {\rm mm}). \quad (10)$$

Note that smaller (and negative) values on this scale represent larger grain sizes. Output grain size distribution for an object does not necessarily, or even typically, represent a Gaussian distribution. Thus, we report the median of this distribution as the best-fit grain size and report upper and lower uncertainties by computing the grain sizes that encompass one standard deviation from the median value. The diurnal e-folding thermal skin depth,[6]

$$l_s = \sqrt{\frac{k_{\rm eff} P_{\rm rot}}{\pi c_s \rho_{\rm grain}(1-\phi)}} = \sqrt{\frac{P_{\rm rot}}{\pi}} \frac{\Gamma}{c_s \rho_{\rm grain}(1-\phi)}, \quad (11)$$

is also computed, and the median and standard deviations from the output distribution are reported.

2.4. Caveats and Model Limitations

For some asteroids in our sample, the material properties inferred from spectroscopy, color, or albedo data may not be correct. For example, incorrect assignment of an asteroid as a metallic M-type when it is actually composed of silicate S-type material is a possible case that could cause nonnegligible change in the grain size estimate. To understand the effects of incorrect classification, we modeled the thermal conductivity model for (22) Kalliope (an M-type) with both metal-rich and S-type properties. Kalliope's low radar albedo may suggest a silicate-rich instead of a metal-dominated surface (Lupishko & Belskaya 1989; Ockert-Bell et al. 2010; Hardersen et al. 2011). Assuming that Kalliope has S-type properties instead of being metal-rich increased its grain size estimate by ~8%, which is *far* below the typical $d_{g\phi}$ uncertainty reported in Section 3.

[6] Both MacLennan & Emery (2019) and Paper I incorrectly quote the formula for l_s by including a factor of $1/\sqrt{2}$, although no values were reported in either work.

From this case, we can reasonably assume that uncertainty in the assumed material properties does not significantly contribute any significant systematic bias in grain sizes.

Both of the thermal conductivity models assume homogeneous, monodispersed grain sizes throughout the surface and constant thermophysical properties with depth. This is also true of reported thermal inertia values. Surface processes that sort grain sizes both vertically and spatially are likely present on asteroids (Richardson et al. 2020, and references therein). Thus, this assumption of regolith homogeneity is certainly not the case for *any* asteroid, and many spacecraft missions have revealed surfaces that are heterogeneous (Figure 1). Specifically, the Hayabusa mission showed that the surface of Itokawa was consistent with the remotely determined thermal inertia (600–800 $\mathrm{J\,m^{-2}\,K^{-1}\,s^{-1/2}}$) yet still contained regions dominated by fine-grained regolith—counter to interpretation of a high thermal inertia (Yano et al. 2006; Müller et al. 2014). Overall, most asteroid regoliths are expected to be heterogeneous, and the assumption of a single grain size and homogeneous regolith is a practical simplification. However, estimates on the spatial heterogeneity of an asteroid surface are limited owing to the fact that we are using disk-integrated (spatially unresolved) observations.

The recent spacecraft visits to two primitive NEAs, Ryugu and Bennu, unexpectedly revealed surfaces that were different from the initial interpretation of their respective thermal remote observations (see Figure 1). The surfaces of these objects exhibited surfaces composed of a significant fraction of large porous boulders that were significantly larger than the grain size estimated from thermal inertia (Grott et al. 2019; Rozitis et al. 2020). Because these boulders have a low thermal conductivity that is similar to a coarse-grained regolith, they exhibit thermal properties indistinguishable from a coarse-grained regolith. Ryan et al. (2020) claimed that the underestimated grain size of Bennu from its thermal inertia can be explained by the inherently low thermal conductivity of Bennu's surface, which resembles CM chondrites and causes nonisothermal effects within the regolith. Grain size estimates are larger when accounting for this nonisothermality and thus can partly explain the large boulders on Bennu and Ryugu.

Because asteroid regoliths are assuredly a mixture of particle sizes, the reported grain size estimates herein should be thought of as a *thermally characteristic* grain size. Furthermore, it is unknown how this grain size relates to the size distribution of regoloith particles. Presley & Craddock (2006) modeled the thermal conductivity of known granular mixtures and deduced that the modeled grain size is most representative of the larger regolith grains—specifically the 85th to 95th percentiles—rather than the mean or modal grain size. On the other hand, Ryan et al. (2020) showed that the particle size from thermal inertia corresponds to within 15% of the mean volumetric particle size for various size–frequency distributions. Additionally, because emitted thermal flux is strongly temperature dependent ($\propto T^4$), it is possible that these thermally characteristic grain sizes are more representative of warmer regolith patches that consist of smaller grains. Another complication could exist owing to the fact that warmer areas emit flux at shorter wavelengths, as opposed to cooler areas that emit more flux at longer wavelengths. Therefore, it is possible that the thermal inertia and thermally characteristic grain sizes are correlated with the wavelength(s) used in the observation(s). Investigation into the relationship between the grain size and regolith particle distribution is beyond this work, and we strongly suggest it as a topic for future studies.

As remarked by Ryan et al. (2020), the apparent thermal inertia will be that of solid rock when the effective particle size is approximately larger than the skin depth, which could be the case for fast rotators with low k_{grain}. If the size range of particles exceeds the skin depth, then the surface is best modeled as a lateral, checkerboard-like mixture of regolith and bare rock (boulders; e.g., Bandfield et al. 2011; Rozitis et al. 2020). Despite these caveats, limitations, and uncertainties of the thermal conductivity model, we claim that the grain sizes derived here are appropriate to identify potential trends among asteroid surfaces.

3. Results and Analysis

We report modeled estimates of grain size and thermal skin depth in Table 5, along with the model input parameters (with associated uncertainties) for each object—Γ, T_{surf}, and spectral type. In some cases, the estimated grain sizes exceed the calculated thermal skin depth (see Section 3.1). In order to caution readers, we mark grain sizes that exceed the 1σ skin depth lower limit with a "*" in Table 5. We find that the Sakatani et al. (2017) thermal conductivity model is incompatible with some of the thermal inertias in which the model overestimates the thermal conductivity. In such cases, only the grain size from the Gundlach & Blum (2013) model is reported. Similarly, we find that several C-type asteroids have very low reported thermal inertias that were incompatible with the assumed thermal conductivity. In these cases, we reran the model with B-type input parameters, which assume a lower value for the thermal conductivity. We mark these objects as "B*" and include them in the assumed B-type group for the post-hoc analyses. Lastly, we have found that the albedos of a few objects in our set are inconsistent with the spectral type of the reported family (Table 1). Similar to Masiero et al. (2013), we thus reject the family membership of these objects and indicate this by crossing through the family name in the rightmost column of Table 5.

We now aim to investigate possible explanatory factors and quantify their influence on the regolith grain size for our subsample of the asteroid population. We test the hypothesis that grain sizes are negatively correlated with asteroid diameter (indicating impact-driven processes) and whether grain size is positively correlated with rotation period (which is caused by thermal fracturing processes). Various multiple-linear (hereafter multilinear) regression models are fit to the MBAs to identify and characterize the dependencies of these factors (Section 3.2). Although the NEAs in this work offer insight into the regolith of very small asteroids, the chaotic nature of changes in their orbital parameters makes it difficult to hold other factors constant—such as thermal environment and impact flux—potentially complicating the multilinear analysis. We perform a separate analysis on NEAs in Section 3.4. In our trend analyses, we use the grain sizes produced by the Gundlach & Blum (2013) thermal conductivity model because the Sakatani et al. (2017) model was unable to provide an estimate for some objects. In general, the Sakatani et al. (2017) grain size estimates are consistently larger than those from the Gundlach & Blum (2013) model, but we claim that the trends we are investigating should still be found among the Sakatani et al. (2017) grain size data set.

Table 5
Grain Size Model Inputs and Results (Excerpt)

Object	$D_{\rm eff}$	p_V	Γ (a)	Source	Tax/Color	$P_{\rm rot}$	$T_{\rm surf}$ (K)	Model Comp.	$d_{g\phi}^{\rm G\&B}$	$d_{g\phi}^{\rm Sak}$	l_s (mm)	Family
(1) Ceres	951 ± 8	$0.100^{+0.004}_{-0.006}$	25^{+15}_{-10}	[T1]	C^2	9.0742	238 ± 15	C (*tiS*)	$0.91^{+2.10}_{-2.47}$	$1.31^{+0.67}_{-0.77}$	12 ± 3.3	
(2) Pallas	536 ± 5	$0.142^{+0.006}_{-0.005}$	30^{+15}_{-15}	[T1]	B^2	7.8132(†)	234 ± 15	B (*S*)	$0.74^{+1.70}_{-1.92}$	$1.24^{+0.60}_{-0.73}$	13.2 ± 3.7	
(3) Juno	254 ± 4	$0.209^{+0.020}_{-0.019}$	70^{+30}_{-40}	[T1]	Sk^2	7.2095	245 ± 15	S (*S*)	$0.11^{+1.47}_{-1.17}$	$-0.19^{+1.13}_{-1.43}$	16 ± 4.7	
(4) Vesta	530 ± 24	$0.394^{+0.011}_{-0.024}$	30^{+10}_{-10}	[T2]	V^2	5.3421	230 ± 10	V (*S*)	$2.14^{+1.07}_{-1.40}$	$1.84^{+0.40}_{-0.63}$	10 ± 2.3	
(6) Hebe	198 ± 3	$0.240^{+0.010}_{-0.010}$	50^{+40}_{-35}	[T3]	S^2	7.2744(†)	205 ± 15	S (*S*)	$-1.39^{+2.10}_{-2.63}$	$-1.49^{+1.00}_{-1.20}$	16.3 ± 5.8	
(8) Flora	142 ± 2	$0.252^{+0.015}_{-0.014}$	50^{+35}_{-30}	[T1]	S^2	12.865	244 ± 15	S (*S*)	$-0.06^{+2.10}_{-2.57}$	$-0.22^{+1.20}_{-1.43}$	19.7 ± 6.4	Flora
(10) Hygeia	441 ± 6	$0.064^{+0.003}_{-0.002}$	50^{+20}_{-25}	[T1]	C^2	27.63	210 ± 15	C (*S*)	$-0.29^{+2.07}_{-2.53}$	$0.14^{+0.83}_{-1.00}$	29 ± 7.8	Hygeia
(16) Psyche	243 ± 25	$0.138^{+0.015}_{-0.015}$	120^{+40}_{-40}	[T4]	X^2	4.1959(†)	212 ± 10	Met (*S*); (*A*)	$-1.96^{+1.13}_{-0.97}$	||	13.3 ± 3	
(18) Melpomene	135 ± 3	$0.234^{+0.019}_{-0.017}$	50^{+15}_{-44}	[T1]	S^2	11.57	236 ± 15	S (*S*)	$1.28^{+1.30}_{-1.13}$	$1.14^{+0.70}_{-0.77}$	15.3 ± 5.2	
(19) Fortuna	219 ± 3	$0.047^{+0.002}_{-0.002}$	40^{+30}_{-15}	[T1]	Ch^2	7.4432	232 ± 15	Ch (*S*)	$0.11^{+2.10}_{-2.50}$	$-0.22^{+1.43}_{-1.60}$	16.8 ± 4.7	

Note. (†) Indicates that the reported $P_{\rm rot}$ value has been rounded to four decimal places. ($\star t$) The reported grain size is larger than the 1σ lower limit of the estimated thermal skin depth. (*a*) Thermal inertia values are in SI units (J m^{-2} K^{-1} $s^{-1/2}$). (*C*) Colors from Tholen (1984) are used. (*e*) The mutual eclipse duration of 4 hr is used to compute thermal skin depth. (*F*) Family association (Table 1) is used. (*O*) Family outlier, with suspected family crossed out in the last column. See text for details. (*A*) Object albedo (Figure 2) is used to infer meteorite connection. (*S*) Reflectance spectrum is used. See above for sources. (*T*) Large thermal inertia is used to infer a metal-rich surface. (*U*) A uniform, rather than a Gaussian, distribution was used for the thermal inertia.

References. (1) SMASS I (Xu et al. 1995); (2) SMASSS II (Bus & Binzel 2002); (3) S3OS2 (Lazzaro et al. 2004); (4) MITHNEOS (Binzel et al. 2019); (4*b*) Tholen 1984; (5) Gietzen & Lacy 2007; (6) Reddy et al. 2012; (7) Jewitt & Hsieh 2006; (8) Chapman & Gaffey 1979; (9) Hardersen et al. 2011. (10) Shepard et al. 2006; (11) Vilas et al. 1998; (12) Fieber-Beyer 2015; (13) E. M. MacLennan et al. 2022, in preparation. [T1] Alí-Lagoa et al. 2020; [T2] Capria et al. 2014; [T3] Marsset et al. 2017; [T4] Matter et al. 2013; [T5] Keihm et al. 2012; [T6] Delbo et al. 2015; [T7] Jiang et al. 2020; [T8] Müller et al. 2004a; [T9] Hanuš 2018; [T10] MacLennan & Emery 2021; [T11] Marciniak et al. 2019; [T12] Marciniak et al. 2018; [T13] MacLennan & Emery 2019; [T14] Yu et al. 2017; [T15] Hanš et al. 2015; [T16] Rozitis et al. 2018; [T17] Pravec et al. 2019; [T18] Rozitis et al. 2013; [T19] Leyrat et al. 2011; [T20] Hanuš 2016; [T21] Rozitis et al. 2014; [T22] Devogèle et al. 2020; [T23] Müller et al. 2004b.

(This table is available in its entirety in machine-readable form.)

3.1. Thermal Skin Depth

First, we review the results for the thermal skin depth l_s of each asteroid in order to place our grain size estimates in better context. As we have mentioned, asteroid surfaces are composed of an unknown mixture of regolith and boulders of various sizes, and it is unknown how the thermal inertia (and characteristic grain size) is representative of this mixture. It is often thought that l_s ought to be considered, in effect, as an upper limit to the size of regolith grains that can be distinguished from bedrock and that particles that are larger than this have effective thermal inertias equal to bedrock (or a boulder that is much larger than l_s). Taking this statement to be truth, we can expect that asteroids with larger l_s should have lower thermal inertias, on average, than those with smaller l_s. However, this expectation is confounded by the fact that rotation period also influences l_s (Equation (11)). To aid our understanding of the relationship between l_s, $P_{\rm rot}$, and Γ, we place the objects in our data set into five rotation period bins (<5 hr, 5–10 hr, 10–20 hr, 20–40 hr, and >40 hr). These rotation period bins are assigned different colors in all three panels of Figure 4. The top panel in this figure shows the distributions of l_s for each rotation period bin. The middle and bottom panels show the thermal inertias and calculated grain sizes as a function of skin depth.

When comparing across the rotation period groups in the top panel of Figure 4, we can see that the two lowest $P_{\rm rot}$ groups have indistinguishable l_s distributions. For the other groups, there is a clear increase in the average l_s among larger rotation periods. Considering this trend, we claim that asteroids with $P_{\rm rot} < 5$ hr have larger-than-expected skin depths. The cause for this is lower thermal inertias among the fast rotators, which is shown in Figure 5 and quantified in our multivariate model fits in Section 3.2. The question now becomes, is the higher thermal inertia among fast rotators a result of shrinking l_s, or caused by an increase in the regolith grain size?

Comparing the thermal inertias and skin depths (middle panel of Figure 4) within the rotation period bins, some interesting findings emerge. Among asteroids with $P_{\rm rot} > 40$ hr, the relationship between thermal inertia and skin depth is roughly what is expected by the proportionality relationship implied by Equation (11), which is shown as a dashed line with an arbitrarily set intercept. Most of the objects with $l_s > 1$ m have very long rotation periods, and this subset of objects, on average, have thermal inertias lower than 300. Asteroids in other rotation bins exhibit a greater dependence of thermal inertia on skin depth than expected from Equation (11), which is possible when the porosity decreases for larger thermal inertia values. Therefore, this trend can be explained if these surfaces are covered with more boulders that have lower porosity than the surrounding regolith. It is also possible that this trend is a result of larger grain sizes, which we consider below.

As the relative contact radii between grains decrease for larger grains, the radiative heat transfer becomes dominant over solid heat transfer through grain contacts. In Paper I we showed that the variation in thermal inertias with temperature is consistent with the theoretical value when radiation is the dominant heat transfer mechanism. Additionally, both the Gundlach & Blum (2013) and Sakatani et al. (2018) models predict that the radiative thermal conductivity component is directly proportional to grain size. Therefore, we can expect that the thermal skin depth increases in proportion to the square root of the grain size or, equivalently, that the grain size is proportional to the square of the skin depth. The lines showing this proportionality in the bottom panel of Equation (11) show that this is indeed the case across our entire data set. Interestingly, it appears that objects with smaller rotation periods exhibit a stronger relationship between the predicted grain size and skin depth. Furthermore, objects with $d_g > l_s$ are more likely to be fast rotators, as 10 out of 15 of these objects have $P_{\rm rot} < 5$ hr. In response to the question posed earlier in this section, we posit that the smaller skin depths caused by

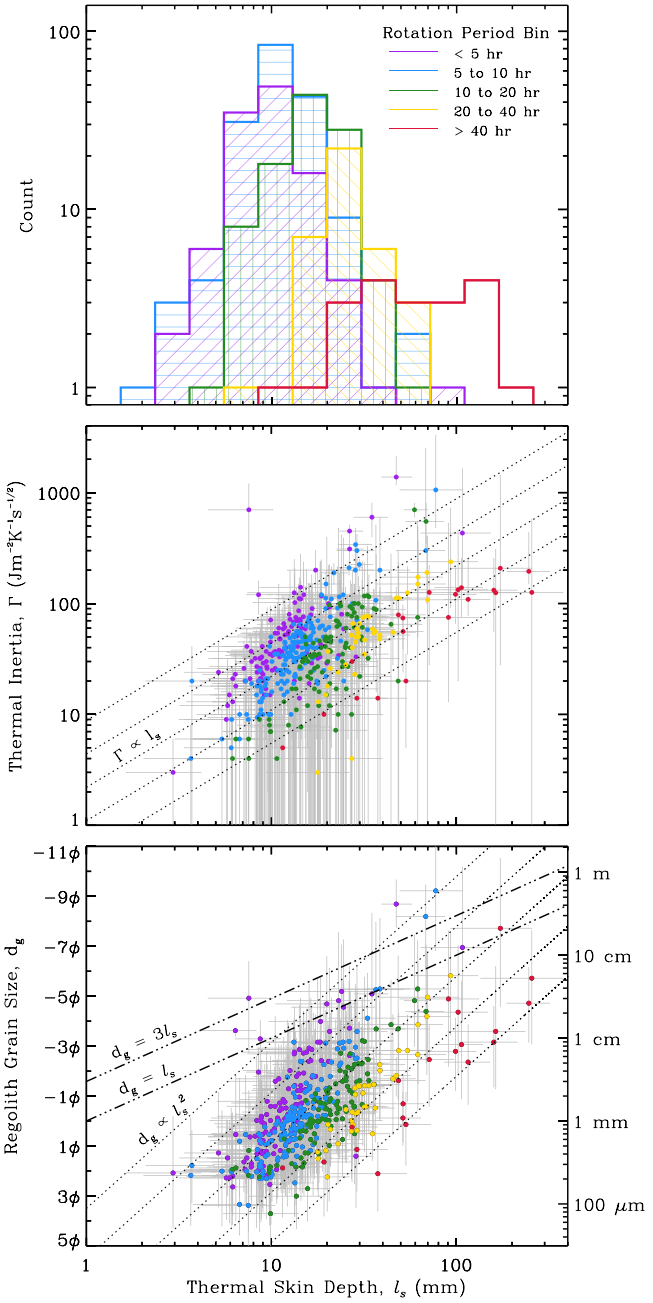

Figure 4. Top: histogram distributions of thermal skin depths, grouped by rotation period. Thermal inertia (middle) and regolith grain size (bottom) are shown as a function of thermal skin depth, with colors indicating rotation period bin defined in the top panel. Dashed lines in the middle and bottom panels show proportionality relationships between the skin depth and thermal inertia or grain size, as shown in each panel. The dashed–dotted–dotted lines indicate where the grain size is equal to the skin depth and three times the skin depth.

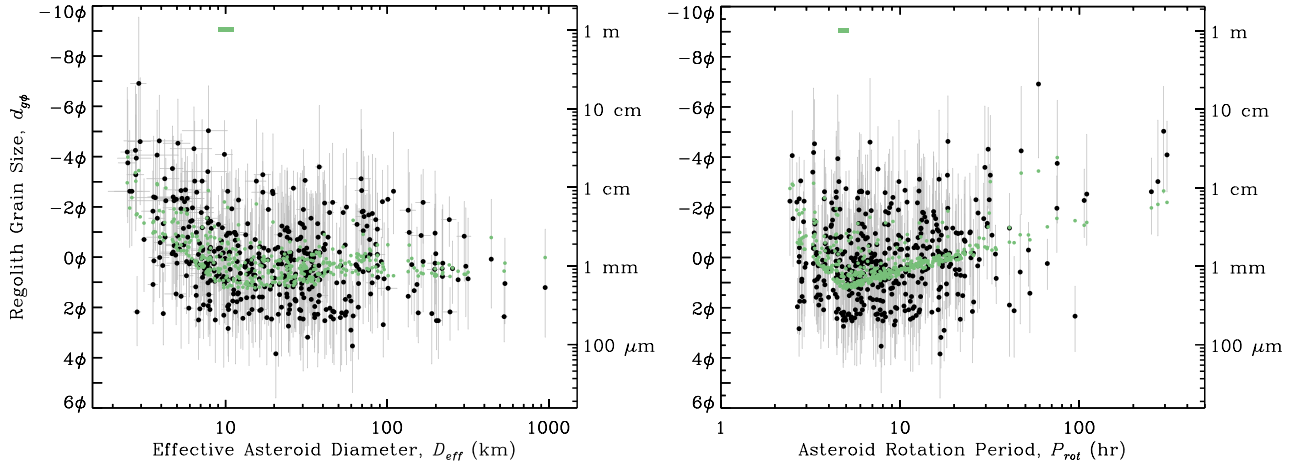

Figure 5. Multilinear model fit *M-4*, shown by colored points, and the grain size data set, shown by black dots, as a function of asteroid diameter (left) and rotation period (right). The colored bars at the top of each panel indicate the 1σ range in uncertainty in the break point between the two segments.

short rotation periods do indeed have a nonnegligible effect on the thermal inertia and resulting regolith grain size. Yet, because most of the grain size estimates for these fast rotators are lower than the skin depth, we claim that this effect is minimal.

3.2. Grain Size Factor Model

Multilinear regression is a method that attempts to model a dependent variable (the grain size, $d_{g\phi}$) as a linear combination of several independent variables—in our case, diameter and rotation period. The fitted slope, or coefficient, of each independent variable and a y-intercept, along with 1σ uncertainties for each of these parameters, is reported. We consider several segmented, or piecewise, multilinear regression models with different numbers and combinations of break points for both independent variables ($D^b_{\rm eff}$ and $P^b_{\rm rot}$), as listed below:

1. *M-1*: no break points.
2. *M-2*: $1 \times D^b_{\rm eff}$.
3. *M-3*: $1 \times P^b_{\rm rot}$.
4. *M-4*: $1 \times D^b_{\rm eff}$, $1 \times P^b_{\rm rot}$.
5. *M-5*: $2 \times D^b_{\rm eff}$.

These segmented models partition the indicated independent variable into intervals for which a different function (slope) is fit to the data. Adding a break point creates two lines that form a continuous, piecewise function in lieu of a single linear fit. In addition to slope estimates of the lines, the locations of the break points are estimated.

The diameter and rotation period are transformed by taking the $\log_{10}$ when used in the multilinear regression models. This variable transformation is done to best capture the wide variance in these variables, which each span more than 2 orders of magnitude. Unlike the thermal inertia multilinear analysis presented in Paper I, we do not consider temperature as an explanatory variable because it is already accounted for in the thermal conductivity model via temperature-dependent heat capacity values (Section 2.2) and radiative heat transport.

We compare the multilinear model fits to one another by taking the adjusted r-squared ($r^2_{\rm adj}$) statistic and Bayesian information criterion (BIC). The $r^2_{\rm adj}$ is a determination of the degree to which the model explains the variance in the dependent variable (i.e., higher values indicate a better fit), while also accounting for the number of predictor parameters, w, in the model. The number of free parameters is calculated from the *total* number of fitted variables, which increases by 2 when a break point is added.[7] The adjusted r-squared is related to r^2 via $r^2_{\rm adj} = 1 - (1 - r^2)(N - 1)/(N - w - 1)$. The BIC is used to indicate which model maximizes the likelihood of matching the data (lower values indicate a higher likelihood) and accounts for the number of model parameters (more parameters increase the score). It can be calculated via $\mathrm{BIC} = N \ln(\mathrm{RSS}) - N \ln(N) + w \ln(N)$, in which RSS is the residual sum of squares (see, e.g., Feigelson & Babu 2012 for more details). Both of these statistics are shown in Table 6, along with the number of model parameters.

When comparing the results among all models, we find that *M-4* has the largest $r^2_{\rm adj}$ and lowest BIC. Statistically speaking, the difference between two model BIC values, ΔBIC, indicates a preference for one over another. Kass & Raftery (1995) state that $\Delta\mathrm{BIC} > 6$ indicates a *strong* preference for the lower BIC. Since *M-4* has a $\Delta\mathrm{BIC} = 34$ between it and the second-lowest BIC value (*M-2*), we use this as an indication that it is the preferred model. We plot the best-fit and preferred *M-4* model in Figure 5. Black symbols are estimated grain sizes for each object, and colored symbols are values from the multilinear models. Solid bars indicate the 1σ range of the diameter and rotation period break points, respectively, at the top of each panel. The estimated intercepts, linear coefficients (slopes), and break point(s) ($D^b_{\rm eff}$, $P^b_{\rm rot}$), along with the associated uncertainties, are listed in Table 7. We remark that the model intercept value represents the predicted $d_{g\phi}$ for a hypothetical object with $D_{\rm eff} = 1$ km and $P_{\rm rot} = 1$ hr, which is just under 1 m for *M-4*.

3.3. Compositional Effects

Here we investigate whether, and by how much, the grain sizes vary or depend on the surface composition of an asteroid. For this analysis we use spectral group as a proxy for composition. Simply comparing the means of the grain size distributions between the groups is not appropriate, as some of the independent explanatory variables are correlated with grain

[7] This is because each new line has a slope and a y-intercept that is independent from others, although a single model intercept is ultimately reported.

Table 6
Comparison of Multilinear Regression Models

Model	w	r^2_{adj}	BIC
M-1	4	0.062	1687
M-2	6	0.141	1660
M-3	6	0.149	1656
M-4	8	0.217	1617
M-5	8	0.141	1670

size: for example, primitive C-complex and P-type bodies are more represented at larger sizes, and the E/Xe-types are largely represented in the lower size range.[8] Instead, we perform post-hoc *t*-tests between the spectral classes by using the model residuals from *M-4*. Since the multilinear analysis does not account for the spectral type, any differences in the group residuals can be used to indicate disparities in regolith grain sizes.

We apply Welch's *t*-test[9] (Welch 1947) in a series of trials between each possible combination of spectral class, as well as between each class and the entire sample with that particular class removed. The null hypothesis that is tested is that the means between the groups do not differ. We report the *p*-values of these trials in Table 8: lower *p*-values indicate a higher probability that the null hypothesis is not supported. Table 8 shows the mean and standard deviation of the model residuals and the number of objects for each group. We analyze the S-, C-, and E-types both with and without the objects in which their spectral type was inferred by their albedo. Similarly, for B-types we analyze both the confirmed B-types and those marked as B* in Table 4 for which we assigned CM meteorite properties based on their low thermal inertias. Consistent with their low thermal inertias, the B* objects have consistently lower grain size residuals compared to confirmed B-types. This may indicate that these objects are not true B-types and may actually be closer in composition to P-types, which have the lowest grain sizes of all the spectral groups included here.

The model residual distributions, grouped by composition, and the mean model residuals are depicted in Figure 6. Compared to the mean of the remainder of the sample, there is strong statistical evidence ($p < 0.01$) that suspected metal-rich asteroids on average exhibit grain sizes that are nearly twice as large as asteroids of the same diameter and rotation period. We interpret this difference as an indication that one of the thermophysical or material properties of FeNi metal affects the efficiency of regolith breakdown process. Additionally, the average grain sizes of M-types and E-types are statistically indistinguishable from one another (Table 8) and from the suspected metal-rich objects. On the other hand, P-types show a much smaller mean grain size than the remainder of the sample ($p < 0.01$). Finally, we note here that S-types and C-types have statistically smaller and larger grain sizes, on average, compared to the rest of the sample. Consistent with this finding, the carbonaceous K-types have coarser-grained regoliths compared to S-types. Potential explanations for these group differences in grain size are discussed in Section 4.

[8] Similar relationships are apparent between spectral classes and heliocentric distance (DeMeo & Carry 2013).

[9] We use Welch's *t*-test, as opposed to the Student's *t*-test, as the latter assumes that the two groups have equal variance or sample size, which is not the case here.

Table 7
Linear Coefficients and Intercept for *M-4*

Parameter	Estimate	1σ Uncertainty	*p*-value
Intercept ($d_{g\phi}$)	−9.85	±1.27	<0.01
D^b (km)	10.1	+1.2/−1.1	<0.01
P^b (hr)	4.84	+0.35/−0.32	<0.01
D^{slope}_{eff} ($<D^b$)	5.27	±0.89	<0.01
D^{slope}_{eff} ($>D^b$)	−0.42	±0.24	0.11
P^{slope}_{rot} ($<P^b$)	7.83	±1.70	<0.01
P^{slope}_{rot} ($>P^b$)	−2.04	±0.28	<0.01

3.4. Near-Earth Asteroids

Thus far in our analysis we have excluded NEAs and Mars crossers (MCs) in order to mitigate the potential influence on regolith evolution caused by widely varying thermal and impact environments. Because these asteroids exhibit a wide range of orbital parameters (varying in both semimajor axis, a, and eccentricity, e), they are subject to drastically varying external influence, whereas we wish to examine the factors inherent to asteroids themselves. We analyze the grain sizes (Section 3) calculated for the NEAs with thermal inertia estimates from other works ($N = 21$) and those estimated in Paper I ($N = 7$). With grain sizes for these 28 asteroids, we seek to identify regolith dependencies on orbital factors.

We perform a multilinear regression model, similar to the one presented in Section 3.2, but with different input factors. We do not consider segmented linear fits, as the low number of objects in this NEA subset may result in model overfitting. The independent explanatory variables we include here are the diameter and rotation period transformed into $\log_{10}$ space. But now we also include the orbital semimajor axis (a), perihelion (q), and aphelion distance (Q) as possible explanatory variables. However, these orbital parameters are *not* transformed into logarithmic space in the multilinear model and are left as is.

The best-fit regression model for NEAs indicated that Q is the only statistically significant variable. Thus, the NEA grain size data set does not appear to show the same trends with the diameter and rotation period that exist among MBAs. On further inspection, potential colinearity between D_{eff} and Q could raise some doubt of the significance of this result. However, employing a multilinear model with only Q and D_{eff} did not change the significance of either variable. We thus conclude that Q is a better predictor of grain size than diameter and rotation period for NEAs. The grain sizes of NEAs as a function of aphelion, perihelion, diameter, and rotation period are shown in Figure 7. Symbol colors indicate the spectral type of the objects, with open symbols indicating that the classification was used using the albedo as a proxy. It is interesting to note here that the grain sizes of objects with 0.9 au $< q <$ 1.1 au are somewhat higher (on average) than the asteroids outside this range and that asteroids with largest grain sizes (>10 cm) are found having perihelia interior to Earth's orbit.

An important caveat to note here is the fact that NEA and MC asteroid diameters extend to a lower size range compared to MBAs. Because the overlap in NEA and MBA diameters occurs for 2 km $< D_{eff} <$ 40 km, it is difficult to draw conclusions about the difference between the two populations from these sets of multilinear models. Grain sizes for NEAs with $D_{eff} > 2$ km

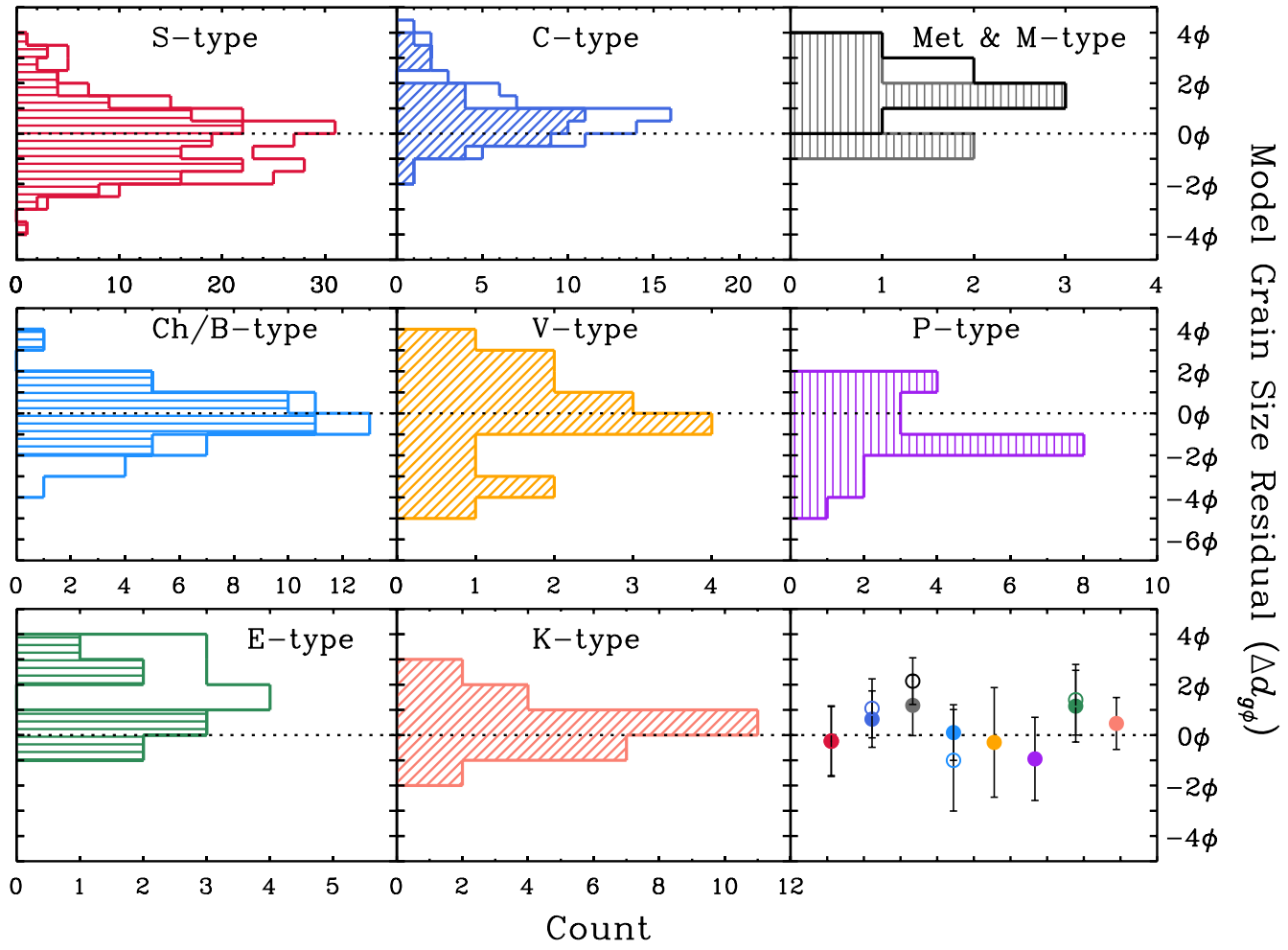

Figure 6. Grain size model residual distributions for different compositional groups and the group means and standard deviations (bottom right panel). Unfilled histograms and open circles in the bottom right panel indicate that objects with assumed spectral classification are included. The filled gray histogram and the black line in the top right panel are for M-types and metal-rich asteroids, respectively. The dotted horizontal line at 0ϕ in each panel is shown for comparison purposes. Note the change in the y-axis range in the middle three panels.

Table 8
Residual Grain Size Statistics and Welch's t-test Results for Different Spectral Groups

		Spectral Group									Assumed Group			
		S	V	C	B	K	E	M	Met	P	S	C	B	E
$\Delta d_{g\phi}$	Mean	−0.24	−0.29	0.63	0.10	0.46	1.15	1.18	2.14	−0.94	−0.24	1.06	−1.00	1.40
	s.d.	1.37	2.17	1.12	1.10	1.03	1.42	1.20	0.92	1.65	1.40	1.16	2.01	1.40
	Count	146	17	49	32	26	8	8	7	23	207	71	42	15
p-value	versus all	<0.01	0.49	<0.01	0.86	0.06	0.06	0.03	<0.01	<0.01	<0.01	<0.01	0.08	<0.01
	S	|	0.92	<0.01	0.14	<0.01	0.03	0.01	<0.01	0.06	0.75	<0.01	0.67	<0.01
	V		|	0.11	0.50	0.20	0.06	0.04	<0.01	0.31	0.86	0.06	0.93	<0.01
	C			|	0.04	0.51	0.36	0.26	<0.01	<0.01	<0.01	0.44	<0.01	0.02
	B				|	0.20	0.08	<0.04	<0.01	0.01	0.19	<0.01	0.13	<0.01
	K					|	0.24	0.16	<0.01	<0.01	<0.01	0.18	<0.01	<0.01
	E						|	0.96	0.13	<0.01	0.03	0.52	0.01	0.46
	M							|	0.10	<0.01	0.01	0.41	<0.01	0.44
	Met								|	<0.01	<0.01	<0.01	<0.01	0.29
	P									|	0.05	<0.01	0.14	<0.01

(Figure 7) are similar to those of similarly sized MBAs and exhibit the same inverse dependency on asteroid diameter. On the other hand, NEAs smaller than 2 km do not show any discernible trend between grain size and asteroid diameter. It is possible that MBAs exhibit a similar lack of trend, but the MBAs in our data set do not extend to this size range.

Additionally, we note that, in general, the comparison between rotation period and grain size for NEAs appears to be

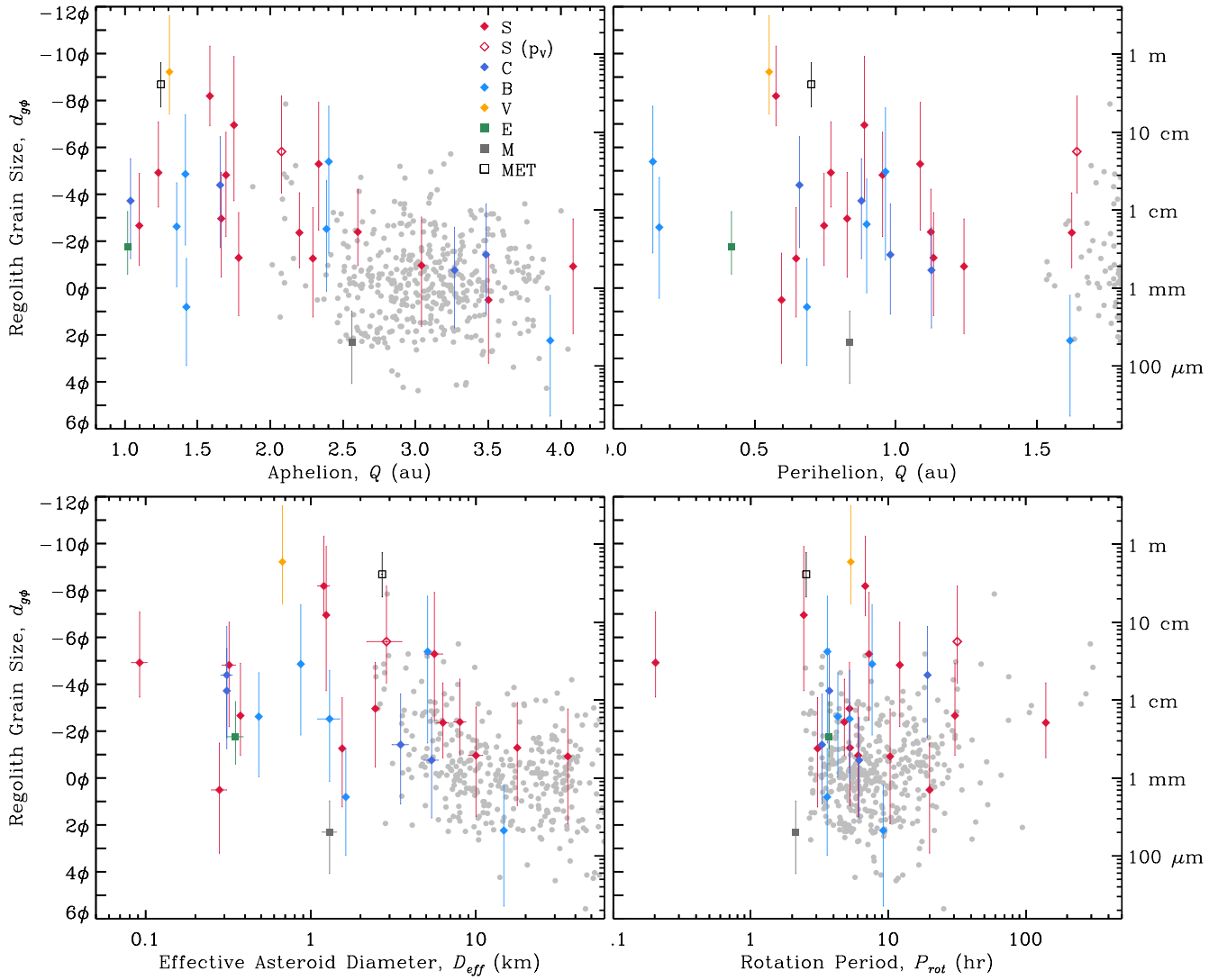

Figure 7. Regolith grain sizes of NEAs as a function of (a) aphelion distance, (b) perihelion distance, (c) asteroid diameter, and (d) rotation period. Symbol colors indicate spectral type as noted in the top left panel and are consistent with previous figures. The open symbols are objects with an inferred spectral type (see text), and gray dots are MBAs.

consistent with MBAs, with a few exceptions. Asteroids with spin rates near the spin barrier ($P_{\rm rot} \approx 2.12$ hr) exhibit a range of grain size spanning 3 orders of magnitude, which mimics the grain size span for MBAs. At the low end of the range is 1950 DA, with two other fast-rotating NEAs exhibiting very large grain sizes. The latter two appear to be very consistent with the inverse trend between rotation period and grain size for MBAs. Thus, 1950 DA appears to be an outlier in this respect, and we further discuss this point below.

4. Discussion

The best-fit multivariate model, *M-4*, indicates that a break point value near ∼10 km occurs in the relationship between asteroid diameter and regolith grain size. The slope fit to objects smaller than this size shows a strong inverse relationship between asteroid diameter and regolith grain size. On average, the regolith grain size of 10 km bodies is 0.6 mm, with *M-4* predicting a grain size of 25 mm for 2 km objects—an increase in $d_{g\phi}$ of nearly a factor of 50, which translates to a power slope of ∼6. The *M-4* slope fit for for asteroids larger than 10 km is statistically indistinguishable from zero, which suggests no dependence of regolith grain size on asteroid diameter. Interestingly, there appears to be an inverse relationship between the upper limit grain size and asteroid diameter among objects larger than ∼80 km. This may indicate a different process or an additional factor that is unaccounted for in our model that influences regolith development on 100 km scale asteroids, which are through to be primordial bodies.

The preferred multilinear model predicts that objects with $P_{\rm rot} \approx 5$ hr, on average, have the smallest grain sizes when comparing across all rotation periods. As the rotation period increases, the model predicts that the grain size increases. Objects rotating faster than ∼5 hr show a steep increase in grain size with decreasing rotation period. It is interesting to note that the model predicts that objects with 2.2 and 300 hr rotation periods should both have $d_g \sim$ 8 mm. These grain size trends with rotation period could indicate at least one regolith evolution process that depends on the spin rates of asteroids. We explore such processes in Sections 4.2 and 4.3. Alternatively, the inverse trend at lower rotation periods could be a result of thermal skin depths that are comparable to the

particle sizes, which we have shown not to be the case in Section 3.1.

4.1. Meteoroid Impact Breakdown

Repeated impacts of smaller asteroids or meteoroids into the surface of an asteroid will create ejecta—some of which is retained at the surface as regolith. The general relationship between the total ejecta mass (M) traveling above a threshold velocity (u), as a function of the impactor's mass and velocity (m and U), is

$$\frac{M}{m} \propto \left(\frac{u}{U}\right)^{-3\tau}, \tag{12}$$

where τ, an empirically derived exponent, is taken as 0.41—the value for sand (Housen & Holsapple 2011). For reference, the probability distribution of relative velocities between asteroids in the main belt has a mode of 4.3 km s^{-1} and a mean value of 5.3 km s^{-1} (Farinella & Davis 1992; Bottke et al. 1994). The velocities of incoming meteoroids are mostly independent of the size of the target body (due to the extremely small gravitational attraction of an asteroid), which leaves the relative size of the impactor to the target asteroid as the dominant factor in Equation (12).

Additionally, the mechanical and structural properties of the target asteroid play a role in determining the outcome (Housen & Holsapple 2003). For example, in targets with low porosity, the ejecta velocities are larger than that of an otherwise identical impact into a porous target (Nakamura & Fujiwara 1991; Nakamura et al. 1994). Energy from the impact is concentrated near the impact site and partitioned into crushing the surface material (Flynn et al. 2015), instead of ejecting it at high velocities. Holsapple et al. (2002) point out that if the porosity of the target region is greater than 50%, only 10% of the crater mass is ejected, as most of the energy is partitioned into compacting the material. This experimental finding was verified by Cambioni et al. (2021), who showed that the presence of fine-grained regolith was less likely to be found surrounding porous boulders on Bennu's surface. The authors claim that the production of fine-grained regolith in the general asteroid population is frustrated by the presence of porous boulders. If the surfaces of B-types contain porous boulders similar to Bennu's, then we might expect a larger grain size compared to S-types, assuming that the latter are composed of low-porosity boulders. Inconsistent with this claim, the grain sizes of S-types and B-types are statistically similar for the asteroids in our sample. This most likely indicates that other factors may be more significant than porosity in determining the production of regolith. Further investigation into this topic should be pursued in future studies.

Using the measured meteorite flux at 1 au, Basilevsky et al. (2013) calculated characteristic lunar boulder survival lifetimes from boulder size–frequency statistics on rims of lunar craters with known ages. They estimated that it takes 25–50 Myr to destroy 50% of a typical 1 m-sized boulder, and after 190–300 Myr, more than 99% of boulders should be completely destroyed. Basilevsky et al. (2015) also extrapolated the lunar timescale to Ceres and Vesta assuming that boulders are broken down exclusively via impact weathering. On these large MBAs the boulder weathering timescale is 3% of the lunar value (i.e., 0.75–1.5 Myr), which is mainly a consequence of the meteorite flux being ~2 orders of magnitude greater in the main belt than at 1 au. In all cases, the remaining fraction of boulders exponentially decreases with time.

This theoretical timescale is significantly shorter than the ages of most asteroid families, although a few young (<1 Myr) families have been identified (e.g., Table 1 in Nesvorný et al. 2015) in the main belt. In principle, asteroids in these young families could theoretically be used to investigate regolith properties of asteroid surfaces that have been reset from an impact. One consideration that must be made is the fact that the small asteroids that exist in these recently formed families are less likely to retain fine-grain regolith particles because of their low surface gravity. Statistically speaking, a 1 km asteroid is expected to experience an average of five catastrophic breakups every 1 Myr (Holsapple et al. 2002), or once every ~200 kyr. This timescale is shorter than the estimated boulder survival timescale (0.75–1.5 Myr) of Basilevsky et al. (2015), so we expect that an MBA of this size would not survive long enough to have much of a developed regolith. On the other hand, a 10 km MBA will survive, on average, 16 Myr (~80 times longer than a 1 km body). The implication that 10 km asteroids exist long enough to develop a regolith through impact degradation is consistent with our grain size results.

Our results show that the differences in grain size for NEAs and MCs are most likely dependent on their orbital parameters. This relationship could be explained by the drastic change in collisional probability and velocities of NEAs with MBAs in the main belt (Bottke et al. 1993). Because an NEA that enters the main belt is traveling relatively slower, the velocity difference between it and a typical MBA will be larger compared to two MBAs with similar orbits. This would theoretically result in a more efficient impact weathering rate for NEAs with $Q \gtrsim 2.2$ au, compared to MBAs of a similar size. However, there is no obvious difference in grain sizes for NEAs and MBAs of similar object sizes. Thus, we suppose that another process is the reason for the grain size dependency on orbital parameters.

Evidence from meteorite impact breccias—fragmented samples of an asteroid collision (Burbine & Binzel 2002)—offers insight into the state of asteroid regolith. These meteorites are formed from the lithification of near-surface material from the heat and pressure of an impact and classified by their texture and presence/absence of clasts (Bischoff et al. 2006). A direct connection to asteroid regolith can be made if they are rich in solar-wind gases that are identified isotopically (McKay et al. 1989). Clasts ranging in size from several hundred microns up to many centimeters have been found in HEDs; carbonaceous, ordinary, and enstatite chondrites; and other stony meteorite regolith breccias (Bischoff et al. 2006, and references within). Interestingly, Bischoff et al. (2006) point out that some aubrites are known to contain large enstatite clasts up to 10 cm in size, as well as metal grains up to 1 cm in size. If the aubrite parent body is matched by an E-type spectrum, then these systematically larger clasts and grains are well matched to the finding that E-types have larger regolith grains than other spectral types.

4.2. Thermal Fatigue Breakdown

The cyclic heating and cooling experienced by asteroid surfaces, as a consequence of time-varying insolation, can result in large spatial temperature gradients within the material. These gradients create heterogeneous thermal stress fields (expansion and contraction) across mineral grain boundaries of a rock

(Molaro et al. 2015). This thermal fatigue process involves the structural weakening of the material from thermal gradients and ultimately results in the breakdown of asteroid regolith. It has been debated whether or not thermal fracturing is a relatively significant weathering mechanism for terrestrial rocks (e.g., Molaro & McKay 2010, and references within), yet Delbo et al. (2014) experimentally demonstrated the effectiveness of this process, in vacuo, on a chip of the Murchison (CM2 carbonaceous chondrite) and Sahara 97210 (L/LL3.2 ordinary chondrite) meteorites. Libourel et al. (2021) performed a follow-up study with these two meteorites and Allende (CV3), where they demonstrated that larger temperature gradients, such as those experienced for low perihelion asteroids, result in greater crack growth rates. Images from the encounter of Bennu by OSIRIS-REx provided widespread evidence of thermal cracking across the surface (Molaro et al. 2020). Convincing evidence from the Moon and Mars (Eppes et al. 2015; Ruesch et al. 2020) indicates that thermal breakdown is efficient on other solar system bodies. Both Molaro et al. (2017) and Ravaji et al. (2019) posit that the efficiency of thermal fracturing is controlled by the maximum thermal stress experienced by the rock, as opposed to the average, so we focus on this quantity in our discussion.

Molaro & Byrne (2012) numerically simulated the amount of internal stress experienced by a rock on Vesta, Mercury, and the Moon's surface. In particular, they estimated the amount of temperature change, per unit time ($\Delta T/\Delta t$), and compared to the temperature gradient ∇T within rocks having orientations at different latitudes on the surface. They found that while a rock on Vesta experienced the largest temporal temperature change, it also had the lowest ∇T—leading to a smaller stress field. This case is opposite to that of the Moon and Mercury, in which ∇T and $\Delta T/\Delta t$ were highly correlated. The modeling efforts of Molaro & Byrne (2012) demonstrated that greater thermal stresses were experienced for rocks experiencing faster sunrises (i.e., shorter rotation periods). The stresses were more pronounced for rock surfaces that faced the rising Sun. Daytime shadowing, especially when occurring just after local sunrise or before local sunset, was also a major contributor to increasing the temperature gradients. The authors also predict that preexisting cracks would contribute even more to the crack growth rate and shorten breakdown timescales.

Our asteroid grain size modeling results indicate that objects with $P_{\rm rot} = 5$ hr are most likely to exhibit the fine-grained regoliths and coarse-grained regoliths ($d_g \gtrsim 1$ cm) are found among the asteroids with $P_{\rm rot} > 100$ hr. This result coincides with the findings of Molaro et al. (2017), El Mir et al. (2019), and Ravaji et al. (2019), as they all predict less efficient thermal fatigue for objects with longer rotation periods. The rotation period break point in the multilinear fit at ~5 hr could be indicative of an optimal rotation rate that maximizes thermal fracturing for asteroid surfaces. The Molaro et al. (2017) model does not predict any rotation period that maximizes the thermal fracturing efficiency, yet El Mir et al. (2019) and Ravaji et al. (2019) found that breakdown timescales for a 10 cm rock are minimized for rotation periods in the range 10–15 hr. It is not immediately obvious why these works predict a slightly larger optimal rotation rate for thermal breakdown. Future works should seek to reconcile thermal fatigue models with our empirical findings.

Molaro et al. (2015) studied the sensitivity of their microstress model to changes in the material properties of the rock and found the thermal expansion coefficient and Young's modulus (which describes tensile elasticity) to be the most influential properties, and that thermal conductivity, perhaps counterintuitively, does not significantly affect the rate of crack growth. The thermal parameter,

$$\Theta = \frac{\Gamma}{\varepsilon \sigma_0 T_{\rm eq}^3} \sqrt{\frac{2\pi}{P_{\rm rot}}}, \tag{13}$$

may intuitively at first seem to be useful in predicting the effectiveness of thermal fatigue on asteroid surfaces, as it can be used as a proxy for the amplitude of the diurnal temperature range. However, its formulation does not capture the essential information regarding the heating and cooling *rates* of a boulder/rock at the surface. For example, regolith on very slow rotators will experience slow sunrises that result in relatively slow rate of temperature change. This behavior may seem paradoxical if one were only to examine the thermal parameter for a hypothetical slow rotator: as $P_{\rm rot}$ increases, Θ becomes smaller and the diurnal temperature range is maximized. However, the rate of temperature change is relatively small for a hypothetical point on the surface of a slow rotator, and the insolation changes experienced during long sunrises and sunsets do not result in spatial temperature gradients large enough to cause significant thermal fracturing.

Our results indicate that the grain sizes of E-type (including assumed E-types), M-type, and suspected metal-rich (Met) asteroids are, on average, ~2 times higher than those of asteroids of the same diameter and rotation period (Figure 5). This suggests either that regolith generation is inefficient for these bodies or that smaller regolith grains are preferentially lost (see Section 4.3). Considering the former, we consider the idea that compositional differences may lead to less efficient breakdown. For example, the relatively high values of Young's moduli for FeNi metal should result in more efficient breakdown via thermal fatigue (Molaro et al. 2015) because stiffer materials are less able to accommodate the differential thermal expansion of grains. This idea is supported if we consider the heterogeneous mesosiderite meteorites, which consist of a silicate-metal mixture, as the appropriate analog for metal-rich bodies. We suspect that greater thermal stresses surrounding silicate grains will lead to efficient thermal fatigue breakdown. Therefore, we suspect that E-types, M-types, and metal-rich bodies are subject to one or more processes that remove smaller particles from their surfaces.

Finally, we remark that thermal fatigue may be a self-limiting process, as long as other processes are insignificant. In this case we claim that an insulating layer of regolith may form over a boulder as a result of thermal fatigue, effectively shielding it from larger temperature gradients. In actuality, impact processes disrupt asteroid surfaces over time and overturn the topmost layers (i.e., impact gardening; Hörz & Schaal 1977). This may lead to regolith stratification over long periods of time, depending on the impact gardening timescale and efficiency relative to thermal breakdown. Therefore, asteroid regolith may become stratified at millimeter or submillimeter length scales, with progressively smaller grains near the surface.

4.3. Regolith Retention and Loss

The discovery and characterization of active asteroids—those that are observed to exhibit mass loss—are direct

evidence that asteroids are subject to processes that remove regolith from their surface. Several potential mechanisms have been proposed, and some remain as only potential explanations of the activity. Jewitt (2012) reviews such mechanisms, which include impact, centrifugal (inertial), and electrostatic ejection. The OSIRIS-REx cameras directly observed particle ejection from Bennu's surface, which Lauretta et al. (2019) posited were caused by thermal fracturing, volatile dehydration, or meteoroid impacts. Other plausible particle ejection mechanisms such as electrostatic charging were ruled out for Bennu but may act on other objects' surfaces. Depending on the physical properties of an asteroid and its orbital location, all of these processes may or may not be relevant or efficient. We also note that each mechanism may alter asteroid surfaces in different ways because their effectiveness is dependent on the grain size.

In addition to generating regolith, meteoroid impacts may also *remove* regolith grains from an asteroid surface. As noted above, the energy from a meteoroid impact on an asteroid surface is partly transferred to individual regolith grains, resulting in a velocity distribution that varies with grain size (Takasawa et al. 2011). As remarked by Lauretta et al. (2019), high-energy impacts into asteroid surfaces (large impactor mass and/or velocity) do not produce ejecta, but instead partition their energy into modifying the target material (e.g., Fiege et al. 2019). The smallest regolith particles have higher velocities and are thus the most likely to be ejected. The upper size limit for particle ejection depends on factors such as the impactor mass and target mass (Equation (12)). These variables can take on a wide range of values varied in order to predict the mass fraction of ejecta that is retained as a function of velocity. The active asteroids (596) Scheila ($D_{\rm eff} \sim 113$ km) and P/2010 R2 (La Sagra) ($D_{\rm eff} \sim 1.4$ km) are suspected to have been subject to impact-induced mass loss due to their single and sudden brightening events (Jewitt 2012).

The material strength of the target plays a vital role in the ejecta outcome. In general, stronger surface materials produce more ejecta, which can escape the gravitational well of the body more easily than an asteroid composed of weaker material. In addition, Matsui & Schultz (1984) show that impacts into brittle (low-temperature) metal will result in fracture and spallation compared to ductile metal at higher temperature. For high-energy impacts, the strength and/or porosity of the object can play a similar role to what the surface material does for low-energy impacts. We expect that ~100 km objects that exhibit larger regolith grains could be stronger and/or less porous than those with smaller regolith grains. This could explain why the suspected metal-rich asteroids in our sample, all of which are >10 km, have larger-than-average grain sizes. Future efforts in mass determination for many asteroids can be used to investigate a potential relationship between the macro-porosity of asteroids and regolith development.

Our results show that, on average, grain sizes for asteroids larger than ~10 km do not show any dependence on object size. On the other hand, the average grain size increases with decreasing asteroid size for objects smaller than 10 km. This size cutoff could be indicative of an abrupt change in the process of regolith breakdown, or, alternatively, may indicate a change in object physical properties (i.e., interior strength) that controls the mass of impact ejecta. Using crater scaling laws, Housen et al. (1979) predict that asteroids in the 1–10 km range should not harbor a significant regolith ($\ll$1 mm thick) owing to a decrease in *both* the strength and gravitational field of bodies of this size. Asteroids with higher strengths have increased ejection velocities, for similar impact scenarios, compared to low-strength objects (Nakamura et al. 1994). Strength could be coincident with the material composition, which could explain why metal-rich bodies, which are presumably stronger, have less fine-grained regolith compared to S-complex and C-complex asteroids.

For fast rotators, the outward centripetal acceleration near their equators is comparable to the downward gravitational acceleration. Regolith grains in these locations therefore exist in a precarious state, and a small perturbation can transfer enough energy to cause the ejection of equatorial material where the effective gravity is near-zero (Guibout & Scheeres 2003). It is difficult to theoretically predict whether this kind of mass loss occurs incrementally, on a grain-by-grain basis, or catastrophically, with large portions ejected at a time (Scheeres 2015). Lauretta et al. (2019) ruled out centrifugal ejection as an ejection mechanism for Bennu, and, to date, centrifugal ejection has not been definitively determined for any active asteroid (Jewitt 2012).

Among small asteroids, the cohesive (e.g., van der Waals) forces between regolith grains smaller than ~1 cm have theoretically (Scheeres et al. 2010) and experimentally (Murdoch et al. 2015) been shown to dominate over gravitational, inertial, and, in some cases, electrostatic forces. Evidence for cohesive forces present on an asteroid surface was found for the 1.3 km NEA (29075) 1950 DA (Rozitis et al. 2014; Gundlach & Blum 2015). Cohesive forces are inversely dependent on the surface area of the regolith grains (Scheeres et al. 2010). This suggests that a regolith composed of smaller grains may be stronger than one composed of larger grains, which has implications for the effectiveness and behavior of potential mass-loss mechanisms. Particles or rocks with low cohesion could be individually ejected, yet interparticle forces can cause the regolith to be more susceptible to large-scale structural failure. In this scenario planes of weakness preferentially form around massive clumps of grains (Sanchez & Scheeres 2020). As these grain structures are held in a higher-energy state, even a small perturbing force that exceeds the yield stress could trigger a landslide (Scheeres et al. 2010), potentially resulting in a catastrophic loss of fine-grained regolith or, more likely, a mixture of regolith and boulders.

The best-fit multilinear model predicts that faster rotators (with $P_{\rm rot} < 5$ hr) have larger regolith grains. Generally speaking, this finding is consistent with thermal breakdown of regolith and/or with centrifugal ejection of smaller grains. Because smaller grains have greater cohesive properties, we slightly favor the former, although it is possible that centrifugal mass loss can affect a wide range of particle sizes. Interestingly, two fast rotators in the sample, (29075) 1950 DA ($D_{\rm eff} \approx 1.3$ km, $P_{\rm rot} \approx 2.12$) and (3554) Amun ($D_{\rm eff} \approx 2.7$ km, $P_{\rm rot} \approx 2.53$ hr), possess regolith characteristics at the extremes of the sample: Amun has a high thermal inertia, suggesting that it may be completely devoid of fine-grained regolith, in contrast to 1950 DA (Rozitis et al. 2014). Amun may have always been lacking any significant regolith, or it could have been similar to 1950 DA in the past. In the latter case, it was subsequently and periodically spun up such that centrifugal forces exceeded any cohesion holding the regolith together, resulting in the loss of fine-grained regolith held together in massive clumps, as described above. In this scenario, we might expect 1950 DA to lose clumps of fine-grained material

as its rotation rate incrementally increases and structural failure occurs within the regolith. More thermal inertia estimates of rapid rotators ($P_{\rm rot} < 3$ hr) may provide greater detail into the efficiency and probability of centrifugal ejection and the cohesive strength of regolith (Rozitis et al. 2014).

Regolith particles can become electrostatically charged when exposed to ionized solar-wind particles, which are primarily composed of positively charged protons (Lee 1996). Solar UV radiation releases photoelectrons from the surface, and a negatively charged "sheath" builds up on the sunlit side of an asteroid. The electrostatic forces that regolith grains experience in this field can *potentially* overcome the cohesive and gravitational forces (Hartzell 2019). For smaller grains, cohesive forces will always dominate, and electrostatic forces are not likely to remove them from the surface. The largest grains, on the other hand, are too heavy to be affected by electrostatic forces. However, there is an optimal size—proportional to $g_a^{1/4}$—for which electrostatic forces overcome cohesive and gravitational forces, resulting in grain levitation (Hartzell & Scheeres 2011). The optimal grain size is estimated by Hartzell & Scheeres (2011) to be around 2–4 cm for an Eros-sized object ($g_a \sim 5 \times 10^{-3}$ m s^{-2}) and 10–30 cm for an Itokawa-sized object ($g_a \sim 8 \times 10^{-5}$ m s^{-2}).

If electrostatic forces dominate over cohesive forces, we would then expect a *positive* correlation between asteroid size and regolith grain size as opposed to an inverse relationship. Although the entire NEA grain size data set does not show any correlation with asteroid size, the subkilometer NEAs in our data set do exhibit a positive correlation between effective asteroid diameter and grain size that is consistent with this expectation. We suspect that regolith processes in this size range become confounded by multiple competing forces, and future modeling could show which process(es) dominate on different bodies.

5. Conclusions and Future Work

In this work we have presented regolith grain size estimates for 452 asteroids (Section 3) and performed a few multilinear model fits to the data set and post-hoc tests between compositional groups and asteroid families. From our results we conclude the following:

Regolith grain size across our sample of MBAs is inversely dependent on object size when the effective diameter is below ~10 km (Section 3.2). We suspect that this relationship is most likely due to the removal of smaller regolith particles via impact processes due to the lower surface gravity of smaller objects. For MBAs larger than ~10 km, regolith grain size does not exhibit any dependence on asteroid size. Additionally, grain size shows a positive dependence on rotation period for $P_{\rm rot} > 5$ hr and an inverse relationship below this value. Nearly all the asteroids with rotation periods above 100 hr are coarse grained with grain sizes >1 cm.

We show that potential metal-rich asteroids have consistently larger regolith grains than objects belonging to other spectral types of similar size and rotation period (Section 3.3). We find that M-types and E-types have coarser-grained regoliths, which may be related to their enstatite content. Finally, the compositionally primitive P-types exhibit lower-than-average regolith grain sizes (more fine grained) than any other spectral type.

The regolith grain sizes of NEAs, which represent asteroid diameters smaller than the MBAs in our sample, are inversely dependent on aphelion (Section 3.4) but not diameter or rotation period. Additionally, the grain sizes of NEAs with aphelia in the main belt are consistent with MBAs with similar aphelia, and the grain sizes of >2 km NEAs are consistent with those of MBAs at the same sizes. Thus, it is not possible to say whether NEAs have different regoliths than MBAs, or if aphelion, rather than size, is a controlling factor of NEA grain sizes.

Finally, we infer from our analyses that evidence for both impact weathering and thermal fatigue/fracture exists in the asteroid population. In future work, processes that remove regolith (Section 4.3), which may preferentially act on smallest regolith particles or largest boulders, should be accounted for when modeling asteroid regolith evolution.

Although the thermal conductivity equations in this work are useful to estimate grain size from thermal inertia, more effort is needed to improve modeling efforts to better resemble asteroid surfaces and regoliths. In particular, considerations for mixed surfaces composed of heterogeneous grains and both solid and porous boulders should be sought (e.g., Cambioni et al. 2019).

Future thermophysical investigations of asteroids should target objects belonging to categories for which there are a relatively low number of thermal inertia estimates, for example, MBAs smaller than ≈3 km, super slow rotators ($P_{\rm rot} > 100$ hr), and members of very young asteroid families (<10 Myr). In addition, thermophysical investigation of the regoliths of object groups not studied in this work (e.g., contact binary asteroids, asteroids with satellites, objects with close planetary encounters, low perihelion asteroids, etc.) would further elucidate regolith evolution processes and their respective timescales.

We appreciate the comments and critiques from two anonymous reviewers that enhanced the quality and efficacy of this article. The authors also thank Dr. Anne Virkki for helpful comments on the manuscript. This work is made possible by funding from the NASA Earth and Space Science Fellowship NNX14AP21H. E.M.M. is partly supported by the Academy of Finland (No. 316292). Article open access funded by Helsinki University Library.

ORCID iDs

Eric M. MacLennan https://orcid.org/0000-0002-9870-123X
Joshua P. Emery https://orcid.org/0000-0001-9265-9475

References

Alí-Lagoa, V., Müller, T., Kiss, C., et al. 2020, A&A, 638, A84
Bandfield, J. L., Ghent, R. R., Vasavada, A. R., et al. 2011, JGRE, 116, E00H02
Basilevsky, A. T., Head, J. W., & Horz, F. 2013, P&SS, 89, 118
Basilevsky, A. T., Head, J. W., Horz, F., & Ramsley, K. 2015, P&SS, 117, 312
Beck, P., Schmitt, B., Potin, S., Pommerol, A., & Brissaud, O. 2021, Icar, 354, 114066
Beech, M., Coulson, I. M., Nie, W., & McCausland, P. 2009, P&SS, 57, 764
Binzel, R. P., DeMeo, F. E., Turtelboom, E. V., et al. 2019, Icar, 324, 41
Bischoff, A., Scott, E. R. D., Metzler, K., & Goodrich, C. A. 2006, in Meteorites and the Early Solar System II, ed. D. S. Lauretta & H. Y. McSween (Tucson, AZ: Univ. Arizona Press), 679
Bottke, W. F. J., Nolan, M. C., & Greenberg, R. 1993, LPSC, 24, 159
Bottke, W. F., Jr., Nolan, M. C., Greenberg, R., & Kolvoord, R. A. 1994, Icar, 107, 255

Burbine, T. H., & Binzel, R. P. 2002, Icar, 159, 468
Burbine, T. H., Binzel, R. P., Bus, S. J., & Clark, B. E. 2001, M&PS, 36, 245
Bus, S. J., & Binzel, R. P. 2002, Icar, 158, 146
Cadenhead, D. A., & Stetter, J. R. 1975, LPSC, 6, 3199
Cambioni, S., Delbo, M., Poggiali, G., et al. 2021, Natur, 598, 49
Cambioni, S., Delbo, M., Ryan, A. J., Furfaro, R., & Asphaug, E. 2019, Icar, 325, 16
Cantillo, D. C., Reddy, V., Sharkey, B. N. L., et al. 2021, PSJ, 2, 95
Capria, M. T., Tosi, F., Sanctis, M. C. D., et al. 2014, GeoRL, 41, 1438
Chan, C. K., & Tien, C. L. 1973, Journal of Heat Transfer, 95, 302
Chapman, C. R., & Gaffey, M. J. 1979, in Asteroids, ed. T. Gehrels & M. S. Matthews (Tucson, AZ: Univ. Arizona Press), 655
Clark, B. E., Bus, S. J., Rivkin, A. S., et al. 2004, JGR, 109, E02001
Clark, B. E., Ockert-Bell, M. E., Cloutis, E. A., et al. 2009, Icar, 202, 119
Consolmagno, G. J., Britt, D. T., & Macke, R. J. 2008, ChEG, 68, 1
Consolmagno, G. J., Schaefer, M. W., Schaefer, B. E., et al. 2013, P&SS, 87, 146
de Kleer, K., Cambioni, S., & Shepard, M. 2021, PSJ, 2, 149
Delbo, M., Libourel, G., Wilkerson, J., et al. 2014, Natur, 508, 233
Delbo, M., Mueller, M., Emery, J. P., Rozitis, B., & Capria, M. T. 2015, in Asteroids IV, ed. P. Michel, F. E. DeMeo, & W. F. Bottke, Jr. (Tucson, AZ: Univ. Arizona Press), 107
DeMeo, F. E., Binzel, R. P., Slivan, S. M., & Bus, S. J. 2009, Icar, 202, 160
DeMeo, F. E., & Carry, B. 2013, Icar, 226, 723
DeMeo, F. E., & Carry, B. 2014, Natur, 505, 629
Devogèle, M., MacLennan, E., Gustafsson, A., et al. 2020, PSJ, 1, 15
Dullien, F. A. L. 1979, Porous Media (New York: Academic),
El Mir, C., Ramesh, K. T., & Delbo, M. 2019, Icar, 333, 356
Elkins-Tanton, L. T., Asphaug, E., Bell, J., et al. 2016, LPSC, 47, 1631
Eppes, M.-C., Willis, A., Molaro, J., Abernathy, S., & Zhou, B. 2015, NatCo, 6, 6712
Farinella, P., & Davis, D. R. 1992, Icar, 97, 111
Feigelson, E. D., & Babu, G. J. 2012, Modern Statistical Methods for Astronomy (Cambridge: Cambridge Univ. Press)
Fieber-Beyer, S. 2015, NASA Planetary Data System. V3.0. EAR-A-I0046-3-FBIRTFSPEC-V3.0, doi:10.26033/zmce-bv77
Fiege, K., Guglielmino, M., Altobelli, N., et al. 2019, JGRE, 124, 1084
Flynn, G. J., Consolmagno, G. J., Brown, P., & Macke, R. J. 2018, ChEG, 78, 269
Flynn, G. J., Durda, D. D., Patmore, E. B., et al. 2015, P&SS, 107, 64
Gietzen, K., & Lacy, C. 2007, LPSC, 38, 1104
Grott, M., Knollenberg, J., Hamm, M., et al. 2019, NatAs, 3, 971
Guibout, V., & Scheeres, D. J. 2003, CeMDA, 87, 263
Gundlach, B., & Blum, J. 2012, Icar, 219, 618
Gundlach, B., & Blum, J. 2013, Icar, 223, 479
Gundlach, B., & Blum, J. 2015, Icar, 257, 126
Hanuš, J., Delbo, M., & Ďurech, J. 2018, Icar, 309, 297
Hanuš, J., Delbó, M., Ďurech, J., & Alí-Lagoa, V. 2015, Icar, 256, 101
Hanuš, J., Delbo, M., & Vokrouhlický, D. 2016, A&A, 592, A34
Hardersen, P. S., Cloutis, E. A., Reddy, V., Mothe-Diniz, T., & Emery, J. P. 2011, M&PS, 46, 1910
Hartzell, C. M. 2019, Icar, 333, 234
Hartzell, C. M., & Scheeres, D. J. 2011, P&SS, 59, 1758
Hazeli, K., El Mir, C., Papanikolaou, S., Delbo, M., & Ramesh, K. T. 2018, Icar, 304, 172
Holsapple, K., Giblin, I., Housen, K., Nakamura, A., & Ryan, E. 2002, in Asteroids III, ed. W. F. Bottke, Jr. et al. (Tucson, AZ: Univ. Arizona Press), 443
Hörz, F., Basilevsky, A. T., Head, J. W., & Cintala, M. J 2020, P&SS, 194, 105105
Horz, F., & Cintala, M. 1997, M&PS, 32, 179
Hörz, F., & Schaal, R. B. 1977, PCE, 10, 3
Housen, K. R., & Holsapple, K. A. 2003, Icar, 163, 102
Housen, K. R., & Holsapple, K. A. 2011, Icar, 211, 856
Housen, K. R., Wilkening, L. L., Chapman, C. R., & Greenberg, R. 1979, Icar, 39, 317
Ibrahim, E.-M. I. 2012, Master's thesis, Univ. Calgary, http://hdl.handle.net/11023/194
Jakosky, B. M. 1986, Icar, 66, 117
Jewitt, D. 2012, AJ, 143, 66
Jewitt, D., & Hsieh, H. 2006, AJ, 132, 1624
Jiang, H., Ji, J., & Yu, L. 2020, AJ, 159, 264
Johnson, K. L., Kendall, K., & Roberts, A. D. 1971, RSPSA, 324, 301
Kass, R. E., & Raftery, A. E. 1995, Journal of the American Statistical Association, 90, 773
Keihm, S., Tosi, F., Kamp, L., et al. 2012, Icar, 221, 395
Krumbein, W. C., & Aberdeen, E. J. 1937, JSedR, 7, 3
Landsman, Z. A., Emery, J. P., Campins, H., et al. 2018, Icar, 304, 58
Lauretta, D. S., Hergenrother, C. W., Chesley, S. R., et al. 2019, Sci, 366, 3544
Lazzaro, D., Angeli, C. A., Carvano, J. M., et al. 2004, Icar, 172, 179
Ledbetter, H. M., & Reed, R. P. 1973, JPCRD, 2, 531
Lee, P. 1996, Icar, 124, 181
Leyrat, C., Coradini, A., Erard, S., et al. 2011, A&A, 531, A168
Libourel, G., Ganino, C., Delbo, M., et al. 2020, MNRAS, 500, 1905
Libourel, G., Ganino, C., Delbo, M., et al. 2021, MNRAS, 500, 1905
Lupishko, D., & Belskaya, I. 1989, Icar, 78, 395
Macke, R. J. 2010, PhD thesis, Univ. Central Florida, http://purl.fcla.edu/fcla/etd/CFE0003424
Macke, R. J., Britt, D. T., & Consolmagno, G. J. 2011a, M&PS, 46, 311
Macke, R. J., Consolmagno, G. J., & Britt, D. T. 2011b, M&PS, 46, 1842
Macke, R. J., Consolmagno, G. J., Britt, D. T., & Hutson, M. L. 2010, M&PS, 45, 1513
Macke, R. J., Opeil, C., & Consolmagno, G. J. 2019, M&PS, 54, 2729
MacLennan, E. M., & Emery, J. P. 2019, AJ, 157, 2
MacLennan, E. M., & Emery, J. P. 2021, PSJ, 2, 161
Magri, C., Ostro, S. J., Rosema, K. D., et al. 1999, Icar, 140, 379
Marciniak, A., Alí-Lagoa, V., Müller, T. G., et al. 2019, A&A, 625, A139
Marciniak, A., Bartczak, P., Müller, T., et al. 2018, A&A, 610, A7
Marsset, M., Carry, B., Dumas, C., et al. 2017, A&A, 604, A64
Masiero, J. R., Mainzer, A. K., Bauer, J. M., et al. 2013, ApJ, 770, 7
Matsui, T., & Schultz, P. H. 1984, LPSC, 89, C323
Matter, A., Delbó, M., Carry, B., & Ligori, S. 2013, Icar, 226, 419
McKay, D. S., Swindle, T. D., & Greenberg, R. 1989, in Asteroids II, ed. R. P. Binzel, T. Gehrels, & M. S. Matthews (Tucson, AZ: Univ. Arizona Press), 617
Milani, A., Spoto, F., Knezevic, Z., Novakovic, B., & Tsirvoulis, G. 2015, in IAU Symp. 318, Asteroids: New Observations, New Models (Cambridge: Cambridge Univ. Press), 28
Molaro, J., & Byrne, S. 2012, JGR, 117, E10011
Molaro, J., Byrne, S., & Le, J.-L. 2017, Icar, 294, 247
Molaro, J. L., Byrne, S., & Langer, S. A. 2015, JGRE, 120, 255
Molaro, J. L., & McKay, C. P. 2010, ESPL, 35, 501
Molaro, J. L., Walsh, K. J., Jawin, E. R., et al. 2020, NatCo, 11, 2913
Mothé-Diniz, T., Carvano, J., Bus, S., Duffard, R., & Burbine, T. 2008, Icar, 195, 277
Müller, T. G., Blommaert, J. A. D. L, Bus, S., Duffard, R., & Burbine, T. 2004a, A&A, 418, 347
Müller, T. G., Hasegawa, S., & Usui, F. 2014, PASJ, 66, 52
Müller, T. G., Sterzik, M. F., Schütz, O., Pravec, P., & Siebenmorgen, R. 2004b, A&A, 424, 1075
Murdoch, N., Sánchez, P., Schwartz, S. R., & Miyamoto, H. 2015, in Asteroids IV, ed. P. Michel, F. E. DeMeo, & W. F. Bottke, Jr. (Tucson, AZ: Univ. Arizona Press), 767
Nakamura, A., & Fujiwara, A. 1991, Icar, 92, 132
Nakamura, A. M., Fujiwara, A., & Kadono, T. 1994, P&SS, 42, 1043
Nesvorný, D., Broz, M., & Carruba, V. 2015, in Asteroids IV, ed. P. Michel, F. E. DeMeo, & W. F. Bottke, Jr. (Tucson, AZ: Univ. Arizona Press), 297
Ockert-Bell, M., Clark, B., Shepard, M., et al. 2010, Icar, 210, 674
Opeil, C. P., Britt, D. T., Macke, R. J., & Consolmagno, G. J. 2020, M&PS, 55, E1
Opeil, C. P., Consolmagno, G. J., & Britt, D. T. 2010, Icar, 208, 449
Opeil, C. P., Consolmagno, G. J., Safarik, D. J., & Britt, D. T. 2012, M&PS, 47, 319
Oszkiewicz, D. A., Bowell, E., Wasserman, L. H., et al. 2012, Icar, 219, 283
Oszkiewicz, D. A., Muinonen, K., Bowell, E., et al. 2011, JQSRT, 112, 1919
Popova, O., Borovika, J., Hartmann, W. K., et al. 2011, M&PS, 46, 1525
Pravec, P., Fatka, P., Vokrouhlický, D., et al. 2019, Icar, 333, 429
Presley, M. A., & Christansen, P. R. 1997, JGR, 102, 6551
Presley, M. A., & Craddock, R. A. 2006, JGR, 111, E09013
Ravaji, B., Alí-Lagoa, V., Delbo, M., & Wilkerson, J. W. 2019, JGRE, 124, 3304
Reddy, V., Le Corre, L., Hicks, M., et al. 2012, Icar, 221, 678
Richardson, J. E., Steckloff, J. K., & Minton, D. A. 2020, Icar, 347, 113811
Rozitis, B., Duddy, S. R., Green, S. F., & Lowry, S. C. 2013, A&A, 555, A20
Rozitis, B., Green, S. F., MacLennan, E., & Emery, J. P. 2018, MNRAS, 477, 1782
Rozitis, B., MacLennan, E. M., & Emery, J. P. 2014, Natur, 512, 174
Rozitis, B., Ryan, A. J., Emery, J. P., et al. 2020, SciA, 6, eabc3699
Ruesch, O., Sefton-Nash, E., Vago, J. L., et al. 2020, Icar, 336, 113431
Ryan, A. J., Pino Muñoz, D., Bernacki, M., & Delbo, M. 2020, JGRE, 125, e06100
Sakatani, N., Ogawa, K., Arakawa, M., & Tanaka, S. 2018, Icar, 309, 13

Sakatani, N., Ogawa, K., Iijima, Y., et al. 2017, AIPA, 7, 015310
Sanchez, J. A., Reddy, V., Bottke, W. F., et al. 2021, PSJ, 2, 205
Sanchez, P., & Scheeres, D. J. 2020, Icar, 338, 113443
Scheeres, D. 2015, Icar, 247, 1
Scheeres, D. J., Hartzell, C. M., Sańchez, P., & Swift, M. 2010, Icar, 210, 968
Shepard, M. K., Margot, J.-L., Magri, C., et al. 2006, Icar, 184, 198
Shoemaker, E. M., Batson, R. M., Holt, H. E., et al. 1969, JGR, 74, 6081
Sih, S. S., & Barlow, J. W. 2004, Particulate Science and Technology, 22, 427
Simpson, E. H. 1951, Journal of the Royal Statistical Society, Series B, 13, 238, http://www.jstor.org/stable/2984065
Soini, A. J., Kukkonen, I. T., Kohout, T., & Luttinen, A. 2020, M&PS, 55, 402
Sunshine, J. M., Thomas, N., El-Maarry, M. R., & Farnham, T. L. 2016, JGRE, 121, 2194
Szurgot, M., Wach, R. A., & Przylibski, T. A. 2012, Metit, 2, 53
Takasawa, S., Nakamura, A. M., Kadono, T., et al. 2011, ApJL, 733, L39
Tholen, D. J. 1984, PhD thesis, Univ. Arizona
van Antwerpen, W., Rousseau, P., & du Toit, C. 2012, NuEnD, 247, 183
Vereš, P., Jedicke, R., Fitzsimmonsand, A., et al. 2015, Icar, 261, 34
Vilas, F., Smith, B. A., McFadden, L. A., et al. 1998, NASA Planetary Data System. EAR-A-3-RDR-VILAS-ASTEROID-SPECTRA-V1.1, doi:10.26033/btr8-vt33
Wach, R. A., Adamus, A., & Szurgot, M. 2013, M&PSA, 48, 5017
Watson, K. 1964, PhD thesis, Caltech, https://resolver.caltech.edu/CaltechETD:etd-11042002-153232
Welch, B. L. 1947, Biometrika, 34, 28
Wood, S. E. 2020, Icar, 352, 113964
Woods-Robinson, R., Siegler, M. A., & Paige, D. A. 2019, JGRE, 124, 1989
Xu, S., Binzel, R. P., Burbine, T. H., & Bus, S. J. 1995, Icar, 115, 1
Yano, H., Kubota, T., Miyamoto, H., et al. 2006, Sci, 312, 1350
Yomogida, K., & Matsui, T. 1983, JGR, 88, 9513
Yu, L. L., Yang, B., Ji, J., & Ip, W.-H. 2017, MNRAS, 472, 2388
Yule, G. U. 1903, Biometrika, 2, 121